



## ATLAS CONF Note

ATLAS-CONF-2020-031

July 30, 2020



# Search for bottom-squark pair production in $pp$ collision events at $\sqrt{s} = 13$ TeV with hadronically decaying tau leptons, $b$ -jets and missing transverse momentum using the ATLAS detector

The ATLAS Collaboration

A search for pair production of bottom squarks in events with hadronically decaying tau leptons,  $b$ -tagged jets and large missing transverse momentum is presented. The analyzed dataset is based on proton–proton collisions at  $\sqrt{s} = 13$  TeV delivered by the Large Hadron Collider and recorded by the ATLAS detector from 2015 to 2018, and corresponds to an integrated luminosity of  $139\text{ fb}^{-1}$ . The observed data are compatible with the expected Standard Model background. Results are interpreted in a simplified model, where each bottom squark is assumed to decay to the second-lightest neutralino  $\tilde{\chi}_2^0$  and a bottom quark, with  $\tilde{\chi}_2^0$  decaying to a Higgs boson and the lightest neutralino  $\tilde{\chi}_1^0$ . The search focusses on final states where at least one Higgs boson decays to a pair of hadronically decaying tau leptons. This allows to significantly improve the acceptance and thus the sensitivity with respect to previous results at low masses of the  $\tilde{\chi}_2^0$ , where bottom-squark masses up to 850 GeV are excluded at the 95% confidence level, assuming a mass difference of 130 GeV between  $\tilde{\chi}_2^0$  and  $\tilde{\chi}_1^0$ .

# 1 Introduction

Although the Standard Model (SM) of particle physics is a very successful theory, it does not provide a natural explanation for the large hierarchy between the energy scale of electroweak interactions and the Planck scale related to the gravitational interaction. Nor does it have a viable candidate particle for dark matter, and it does not include a quantum description of gravity. Supersymmetry (SUSY) [1–6] is a theoretical framework that extends the SM by introducing partner states for the known particles that have the same quantum numbers but differ in spin by half a unit. This leads to a cancellation of loop corrections to the Higgs boson mass, thereby solving the hierarchy problem [7–10]. When conservation of  $R$ -parity [11] is assumed, the lightest supersymmetric particle is stable and would be a viable candidate for dark matter if it is weakly interacting [12, 13]. However, SUSY must be a broken symmetry in order to allow the supersymmetric particles to be heavier than their SM partners and evade detection so far. Naturalness arguments [14, 15] support the assumption that the partner states of the third-generation quarks, the top squark  $\tilde{t}$  and the bottom squark  $\tilde{b}$ , should be light and thus have relatively large production cross sections. They might even be the only strongly-produced supersymmetric states within the current mass reach of the LHC.

This note presents a search for pair production of bottom squarks  $\tilde{b}$  that decay via the second-lightest neutralino  $\tilde{\chi}_2^0$  to the lightest neutralino  $\tilde{\chi}_1^0$ . The neutralinos  $\tilde{\chi}_{1,2,3,4}^0$  together with the charginos  $\tilde{\chi}_{1,2}^\pm$  are mixtures of the partner states of the electroweak gauge bosons (bino and winos) and Higgs bosons (higgsinos). The simplified model [16–18] of production and decay of supersymmetric particles considered in this search is shown in Figure 1. It is inspired from the minimal supersymmetric standard model [19, 20] in scenarios where the branching ratio  $\mathcal{B}(\tilde{\chi}_2^0 \rightarrow h\tilde{\chi}_1^0)$  is enhanced, e.g. when the  $\tilde{\chi}_1^0$  is bino-like and the  $\tilde{\chi}_2^0$  a wino-higgsino mixture. The branching ratio  $\mathcal{B}(\tilde{b} \rightarrow b\tilde{\chi}_2^0)$  is large compared to that of the direct decay  $\mathcal{B}(\tilde{b} \rightarrow b\tilde{\chi}_1^0)$ , which is studied elsewhere [21], when the mixture of the bottom squark is such that it is mostly the superpartner of the left-chiral bottom quark, the  $\tilde{\chi}_1^0$  is mostly bino, and the  $\tilde{\chi}_2^0$  mostly wino. A wino- or higgsino- like  $\tilde{\chi}_2^0$  will be accompanied by a  $\tilde{\chi}_1^\pm$ , which allows the decay  $\tilde{b} \rightarrow t\tilde{\chi}_1^\pm$ . This decay mode is relevant if the mass difference of the bottom squark and the chargino is larger than the top-quark mass. In the simplified model,  $\mathcal{B}(\tilde{b} \rightarrow b\tilde{\chi}_2^0)$  and  $\mathcal{B}(\tilde{\chi}_2^0 \rightarrow h\tilde{\chi}_1^0)$  are assumed to be 100%. Besides, the Higgs boson is assumed to have the same properties as in the SM, namely  $m(h) = 125$  GeV,  $\mathcal{B}(h \rightarrow b\bar{b}) = 58\%$ , and  $\mathcal{B}(h \rightarrow \tau^+\tau^-) = 6.3\%$ . Only decays of the Higgs bosons to  $b\bar{b}$ ,  $\tau^+\tau^-$ ,  $W^+W^-$  and  $ZZ$  are considered in the signal-model generation. Furthermore, the mass difference  $\Delta m(\tilde{\chi}_2^0, \tilde{\chi}_1^0)$  between the  $\tilde{\chi}_2^0$  and  $\tilde{\chi}_1^0$  is set to 130 GeV such that the Higgs boson produced in the decay of the  $\tilde{\chi}_2^0$  is on its mass shell. The free parameters of the model are chosen to be the masses  $m(\tilde{b})$  and  $m(\tilde{\chi}_2^0)$ .

The signal model illustrated in Figure 1 yields a final state with two bottom quarks, two Higgs bosons, and missing transverse momentum from the two  $\tilde{\chi}_1^0$  that escape the detector without interacting. This analysis selects a final state with a pair of tau leptons arising from the decay of one of the Higgs bosons, such that it complements a previous ATLAS search [22], which focusses on final states with multiple  $b$ -jets. It is the first bottom-squark search to exploit this particular decay mode of the Higgs boson. The neutrinos from the tau-lepton decays provide an additional source of missing transverse momentum on top of the pair of  $\tilde{\chi}_1^0$ . This increases the acceptance of the search in the region of parameter space where the  $\tilde{\chi}_2^0$  is relatively light and the  $\tilde{\chi}_1^0$  moderately boosted, where the previous ATLAS analysis has limited sensitivity. The same simplified model has been employed by the CMS collaboration in a search targeting  $h \rightarrow \gamma\gamma$  decays [23]. Using a dataset of  $77.5 \text{ fb}^{-1}$ , this interpretation excludes bottom-squark masses up to 530 GeV

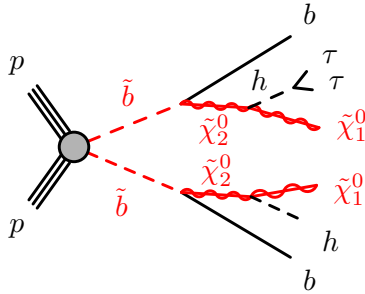


Figure 1: Simplified model of bottom-squark pair production and the decay chain targeted by this analysis.

for an almost massless  $\tilde{\chi}_1^0$  at the 95% confidence level, and bottom-squark masses up to at least 400 GeV for heavier masses of the  $\tilde{\chi}_1^0$ .

The note is structured as follows: after this introduction, Section 2 briefly describes the ATLAS detector, and Section 3 presents the dataset and simulated event samples. The reconstruction of physics objects is described in Section 4, and the signal selection and analysis discriminants are detailed in Section 5. The procedures to derive the background estimate are explained in Section 6, followed by a summary of the systematic uncertainties in Section 7. Section 8 presents the results from the analysis and their interpretation, and conclusions are given in Section 9.

## 2 ATLAS detector

The ATLAS experiment [24–27] at the LHC is a multi-purpose particle detector with a forward-backward symmetric cylindrical geometry and nearly  $4\pi$  coverage in solid angle.<sup>1</sup> It consists of an inner tracking detector surrounded by a thin superconducting solenoid providing a 2 T axial magnetic field, electromagnetic and hadron calorimeters, and a muon spectrometer. The inner tracking detector covers the pseudorapidity range  $|\eta| < 2.5$ . It consists of silicon pixel, silicon microstrip, and transition radiation tracking detectors. Lead/liquid-argon (LAr) sampling calorimeters provide electromagnetic (EM) energy measurements with high granularity. A hadron (steel/scintillator-tile) calorimeter covers the central pseudorapidity range ( $|\eta| < 1.7$ ). The end-cap and forward regions are instrumented with LAr calorimeters for both EM and hadronic energy measurements up to  $|\eta| = 4.9$ . The muon spectrometer surrounds the calorimeters and is based on three large air-core toroidal superconducting magnets with eight coils each. The muon spectrometer includes a system of precision tracking chambers and fast detectors for triggering. A two-level trigger system is used to select events. The level-1 trigger is implemented in hardware and uses information from the calorimeters and the muon spectrometer to accept events at a maximum rate of 100 kHz. This is followed by a software-based high-level trigger (HLT) that reduces the event rate to 1 kHz on average depending on the data-taking conditions.

<sup>1</sup> ATLAS uses a right-handed coordinate system with its origin at the nominal interaction point (IP) in the center of the detector and the  $z$ -axis along the beam pipe. The  $x$ -axis points from the IP to the center of the LHC ring, and the  $y$ -axis points upwards. Cylindrical coordinates  $(r, \phi)$  are used in the transverse plane,  $\phi$  being the azimuthal angle around the  $z$ -axis. The pseudorapidity is defined in terms of the polar angle  $\theta$  as  $\eta = -\ln \tan(\theta/2)$ . Angular distance is measured in units of  $\Delta R \equiv \sqrt{(\Delta\eta)^2 + (\Delta\phi)^2}$ .

### 3 Data and simulated event samples

The dataset used in this analysis consists of proton–proton collision data collected with the ATLAS detector during the second run of the LHC from 2015 to 2018 at a center-of-mass energy of  $\sqrt{s} = 13$  TeV and with a minimum separation of 25 ns between subsequent crossings of proton bunches from the two beams. After applying data-quality requirements that ensure that all detector subsystems were operational, the total integrated luminosity of this data sample is  $139\text{ fb}^{-1}$  with an uncertainty of 1.7% [28], obtained using the LUCID-2 detector [29] for the primary luminosity measurements.

The SUSY signal and SM background processes are modeled with Monte Carlo (MC) simulations, except for the multijet background which is estimated from data. The modelling of the two dominant SM background processes, namely top-quark and  $Z(\tau\tau)$  production, is improved by normalizing their contributions to data as described in Section 6. Simulated samples are produced using the ATLAS simulation infrastructure [30] with either a full simulation of the ATLAS detector in GEANT4 [31], or a faster variant that relies on a parameterized response of the calorimeters [32]. The effect of multiple interactions in the same and neighboring bunch crossings (pile-up) is modeled by overlaying simulated inelastic  $pp$  collisions generated with PYTHIA v8.186 [33] using the NNPDF2.3LO set of parton distribution functions (PDF) [34] and the A3 set of tuned parameters (tune) [35] over the original hard-scattering event. Simulated event samples are weighted to reproduce the amount of pile-up interactions observed in the data. For all simulated samples except those generated with SHERPA [36], the EvtGEN [37] program is used to simulate the decays of bottom and charm hadrons.

The production of  $t\bar{t}$  events is modeled using the PowHEGBox v2 generator [38–41] at next-to-leading order (NLO) in QCD with the NNPDF3.0NLO PDF set [42] and the  $h_{\text{damp}}$  parameter<sup>2</sup> set to  $1.5\text{ }m_{\text{top}}$  [43]. The parton shower, hadronization, and underlying event are modeled with PYTHIA v8.230 [44], using the A14 tune [45] and the NNPDF2.3LO PDF set. The  $t\bar{t}$  sample is normalized to the cross-section prediction at next-to-next-to-leading order (NNLO) in QCD including the resummation of next-to-next-to-leading logarithmic (NNLL) soft-gluon terms calculated using Top++2.0 [46–52].

The associated production of top quarks with  $W$  bosons is modeled using the PowHEGBox v2 generator [39–41, 53] at NLO in QCD using the five-flavor scheme. Single-top-quark production in the  $t$ -channel is modeled using the PowHEGBox v2 generator [39–41, 54] at NLO in QCD using the four-flavor scheme. The  $s$ -channel production is modeled using the PowHEGBox v2 generator [39–41, 55] at NLO in QCD in the five-flavor scheme. For all three channels, the NNPDF3.0NLO PDF set is used for the matrix elements calculation. The events are interfaced with PYTHIA v8.230 using the A14 tune and the NNPDF2.3LO PDF set.

The  $t\bar{t}X$  production ( $X = W, Z, h$ ) is modeled using the MADGRAPH5\_aMC@NLO v2.3.3 generator [56] at NLO in QCD with NNPDF3.0NLO PDFs. The events are interfaced to PYTHIA v8.210 using the A14 tune and the NNPDF2.3LO PDF set.

The production of  $V+\text{jets}$  ( $V = W, Z$ ) is simulated with the SHERPA v2.2.1 generator [36] using NLO matrix elements for up to two jets, and leading-order (LO) matrix elements for up to four jets calculated with the Comix [57] and OpenLoops libraries [58, 59]. They are matched with the SHERPA parton shower [60] using the MEPS@NLO prescription [61–64] using the tune developed by the SHERPA authors. The NNPDF3.0NNLO PDF set [42] is used and the samples are normalized to a NNLO prediction [65].

---

<sup>2</sup> The  $h_{\text{damp}}$  parameter is a resummation damping factor and one of the parameters that controls the matching of Powheg matrix elements to the parton shower and thus effectively regulates the high- $p_{\text{T}}$  radiation against which the  $t\bar{t}$  system recoils.

The SUSY signal samples are generated with `MADGRAPH5_aMC@NLO` v2.2.3 [56] using NNPDF2.3LO PDFs, and the modeling of the parton showering, hadronization and underlying event is performed with `PYTHIA` v8.210 with the A14 tune. The LO matrix elements include the emission of up to two additional partons. The matching between parton shower and matrix elements is done with the CKKW-L prescription [66, 67], with a matching scale set to one quarter of the mass of the bottom squark. Signal samples are generated with bottom-squark masses  $m(\tilde{b})$  ranging from 250 GeV to 1000 GeV, and masses of the second-lightest neutralino  $m(\tilde{\chi}_2^0)$  between 131 GeV and 380 GeV. Signal cross sections are calculated to approximate NNLO in QCD, adding the resummation of soft gluon emission at NNLL accuracy [68–75]. The nominal cross sections and their uncertainties are derived using the `PDF4LHC15_mc` PDF set, following the recommendations of Ref. [76], and decrease from  $(24.8 \pm 1.7) \text{ pb}$  at  $m(\tilde{b}) = 250 \text{ GeV}$  to  $(14.5 \pm 1.5) \text{ fb}$  at  $m(\tilde{b}) = 900 \text{ GeV}$ .

## 4 Event reconstruction

In this section, the reconstruction of the analysis objects from the detector data is described. The search presented in this note is based on events which have  $b$ -jets, hadronically decaying tau leptons and large missing transverse momentum in the final state. In addition to these, selections are used where tau leptons are substituted with muons to improve the background model.

Inner-detector tracks with  $p_T > 500 \text{ MeV}$  are used to reconstruct primary vertices [77]. If several vertex candidates are found, the one with the largest sum of the squared transverse momentum of associated tracks  $\Sigma p_T^2$  is treated as the hard-scattering vertex.

An anti- $k_t$  clustering algorithm [78, 79] with a radius parameter of  $R = 0.4$  is used to reconstruct jet candidates in the calorimeter. Jets are built from massless positive-energy topological clusters [80] of calorimeter cells containing energy above noise threshold measured at the electromagnetic energy scale. The jet candidates are calibrated using jet-energy-scale (JES) corrections derived from data and simulation [81]. A global sequential calibration procedure is applied to improve the jet energy resolution (JER). Jets with  $p_T > 20 \text{ GeV}$  and  $|\eta| < 2.8$  are selected, and a set of quality criteria is applied to reject jets not originating from  $pp$  collisions [82]. To suppress jets from pile-up interactions, a jet-vertex-tagging algorithm [83] is employed for jets with  $p_T < 120 \text{ GeV}$  and  $|\eta| < 2.5$ . Jets containing  $b$ -hadrons are tagged as  $b$ -jets using a Boosted Decision Tree (BDT) algorithm that exploits the impact parameters of tracks within the jet as well as secondary vertex information [84, 85]. The optimal working point for this analysis has an efficiency of 77%, with an approximate misidentification probability of 20% for jets arising from charm quarks, 6.7% for hadronically decaying tau leptons, and 0.9% for light-flavor jets.

The reconstruction of hadronically decaying tau leptons ( $\tau_{\text{had}}$ ) [86] is seeded by anti- $k_t$  jets ( $R = 0.4$ ) built from topological clusters calibrated with a local hadronic weighting scheme [87]. Tau leptons are built from clusters and tracks found within  $\Delta R = 0.2$  of the seed jet axis. The tracks are selected by a set of BDTs, and only the candidates with one or three associated tracks and a charge sum of  $\pm 1$  are considered. Tau leptons are required to have  $p_T > 20 \text{ GeV}$ ,  $|\eta| < 2.5$ , and the transition region between barrel and end-cap calorimeters ( $1.37 < |\eta| < 1.52$ ) is excluded. The energy calibration is based on a Boosted Regression Tree that exploits energy and shower-shape measurements from the calorimeter, information from particle-flow reconstruction [88] and the number of pile-up interactions. A recurrent neural network algorithm [89] is used to separate jets and tau leptons. It uses as input a set of high-level variables combining tracking and calorimeter measurements, as well as low-level variables from individual tracks and clusters. The *loose* identification working point is applied, corresponding to efficiencies of 85% and 75% for 1-prong

and 3-prong tau leptons, respectively. To reduce background from electrons that are misidentified as tau leptons, tau-lepton candidates are discarded if a close-by electron passes the *very loose* working point of the likelihood-based algorithm used to identify electrons. This requirement is tuned to have an efficiency of 95% for hadronically decaying tau leptons [90].

Muon candidates are reconstructed by matching tracks from the inner tracking detector and the muon spectrometer [91]. They are required to have  $p_T > 10 \text{ GeV}$  and  $|\eta| < 2.7$ , to satisfy the *medium* identification criteria, and to pass a  $|z_0 \sin \theta| < 0.5 \text{ mm}$  requirement on the longitudinal impact parameter.<sup>3</sup> After discarding the candidates failing the *overlap-removal* procedure described below, stricter requirements are applied: muons must have  $p_T > 25 \text{ GeV}$ , pass the *loose* isolation criteria and satisfy the requirement  $|d_0|/\sigma(d_0) < 3$  on the transverse impact parameter  $d_0$  and its uncertainty  $\sigma(d_0)$ .

Electron candidates are reconstructed by matching energy clusters in the electromagnetic calorimeter to tracks from the inner tracking detector [92]. A requirement on the longitudinal impact parameter  $|z_0 \sin \theta| < 0.5 \text{ mm}$  discards electrons not associated with the primary vertex. Electrons are included in the missing transverse momentum computation and in the overlap-removal procedure, but are not used otherwise.

The missing transverse momentum vector  $\vec{p}_T^{\text{miss}}$  is defined as the negative vector sum of the transverse momenta of all reconstructed objects mentioned above, with an additional soft term including all tracks from the primary vertex that are not associated with a reconstructed object [93]. The magnitude of  $\vec{p}_T^{\text{miss}}$  is denoted by  $E_T^{\text{miss}}$ .

An overlap-removal procedure is performed after event reconstruction to resolve ambiguities when a single physical object is reconstructed as multiple final-state objects. If two electrons share the same track, the electron with lower transverse momentum is discarded. Tau leptons overlapping with an electron or a muon within  $\Delta R_y \equiv \sqrt{(\Delta y)^2 + (\Delta \phi)^2} < 0.2$  are removed. If an electron and a muon share the same inner-detector track, the muon is removed if it is tagged as a minimum-ionizing particle in the calorimeter, otherwise the electron is discarded. If a jet overlaps with an electron or a muon candidate within  $\Delta R_y < 0.2$ , the jet is removed. An exception is when a jet that has more than two associated tracks overlaps with a muon within  $\Delta R_y < 0.2$ , in which case the jet is kept and the muon is discarded. Finally, electron and muon candidates within  $0.2 < \Delta R_y < 0.4$  of a jet and jets within  $\Delta R_y < 0.2$  of a tau-lepton candidate are discarded.

The same reconstruction and identification algorithms are used for both data and simulation, and dedicated correction factors are applied to account for differences in efficiencies and energy calibrations.

## 5 Event selection

All selections used in this analysis require events to pass a  $E_T^{\text{miss}}$  trigger [94] or a combined  $E_T^{\text{miss}} + b$ -jet trigger, except for specific selections used for the background estimate which rely on single-muon or single-jet triggers as described in Section 6. The  $b$ -jet and muon objects reconstructed by the trigger algorithms are required to geometrically match the corresponding reconstructed analysis objects defined in Section 4, otherwise the event is discarded. The HLT threshold of the  $E_T^{\text{miss}}$  trigger increases from 70 to 110 GeV over the data-taking period. The  $E_T^{\text{miss}} + b$ -jet trigger has HLT thresholds of 60 GeV on  $E_T^{\text{miss}}$

---

<sup>3</sup> The transverse impact parameter is defined as the distance of closest approach in the transverse plane between a track and the beam-line. The longitudinal impact parameter corresponds to the  $z$ -coordinate distance between the point along the track at which the transverse impact parameter is defined and the primary vertex.

Table 1: Summary of the common analysis preselection. The requirements in the upper part of the table apply to all analysis regions, those in the lower part of the table to all but the  $Z(\tau\tau)$  control regions as discussed in Section 6.

$N_\tau + N_\mu$	$\geq 1$
$N_{\text{jets}}$	$\geq 3$
$p_T(\text{jet}_1)$	$> 140 \text{ GeV}$
$p_T(\text{jet}_2)$	$> 100 \text{ GeV}$
$\Delta\phi(\text{jet}_{1,2}, \vec{p}_T^{\text{miss}})$	$> 0.5$
$N_{b\text{-jets}}$	$\geq 2$
$p_T(b\text{-jet}_1)$	$> 100 \text{ GeV}$
Trigger	$E_T^{\text{miss}} + b\text{-jet}$
$E_T^{\text{miss}}$	$> 160 \text{ GeV}$
	OR
	$E_T^{\text{miss}}$
	$> 200 \text{ GeV}$

and 80 GeV on the transverse momentum of the  $b$ -jet, and the efficiency of the online  $b$ -jet identification algorithm determined for simulated  $t\bar{t}$  events is 60% in 2016 and 50% in 2017 and 2018. This trigger increases the acceptance to low- $E_T^{\text{miss}}$  signals expected from low-mass bottom squarks. The dataset associated with the  $E_T^{\text{miss}} + b$ -jet trigger has a reduced integrated luminosity of  $127 \text{ fb}^{-1}$  because the trigger was not active in 2015, and stricter data-quality requirements are applied to  $b$ -jet triggers in 2016 and 2017 due to beam-spot considerations.

Events are rejected if no primary vertex with at least two tracks is found or if they contain a jet failing the *loose* quality criteria described in Ref. [82]. Furthermore, events are rejected if they contain muons with a large uncertainty on the track curvature or muons which are likely to originate from cosmic rays as indicated by a large displacement from the primary vertex.

Events are required to have at least three jets, among which at least two must be  $b$ -tagged unless stated otherwise. The leading and sub-leading jets are required to have  $p_T > 140 \text{ GeV}$  and  $p_T > 100 \text{ GeV}$ , respectively, and the leading  $b$ -jet is required to have  $p_T > 100 \text{ GeV}$ . The  $E_T^{\text{miss}}$  requirement depends on the trigger considered: the  $E_T^{\text{miss}} + b$ -jet trigger reaches maximum efficiency for  $E_T^{\text{miss}} > 160 \text{ GeV}$ , while the  $E_T^{\text{miss}}$  trigger requires  $E_T^{\text{miss}} > 200 \text{ GeV}$  to be fully efficient.

To suppress the multijet background, events are vetoed if the angular separation in the transverse plane  $\Delta\phi(\text{jet}_{1,2}, \vec{p}_T^{\text{miss}})$  between one of the two leading jets and  $\vec{p}_T^{\text{miss}}$  is less than 0.5. All analysis selections require the presence of at least one tau lepton or one muon in the event. This common preselection is summarized in Table 1. In the following, the number of objects in an event is generically written as  $N_{\text{object}}$ , and indices ‘1’ and ‘2’ refer to the leading and sub-leading objects, respectively, which are ordered by decreasing transverse momentum.

On top of the preselection from Table 1, a set of signal regions (SRs) is defined to target the bottom-squark signal processes illustrated in Figure 1. All SRs require at least two hadronically decaying tau leptons with opposite electric charge (referred to as OS criterion) and no muon to be present.

Additional kinematic selections are applied to suppress the SM background. These selections are described in the following and summarized in Table 2. They are optimized by maximising the signal significance [95] in the previously non-excluded parameter space of the targeted signal model.

The visible invariant mass of the two leading tau leptons must be compatible with a Higgs boson decay, and is required to be within  $55 \text{ GeV} < m(\tau_1, \tau_2) < 120 \text{ GeV}$ . The lower bound suppresses the  $Z(\tau\tau)$  background, while the upper bound reduces “non-resonant” background contributions where the tau

leptons do not originate from the same resonance. Events are required to have  $H_T > 1100 \text{ GeV}$ , where  $H_T \equiv \sum p_T^\tau + \sum p_T^\mu + \sum p_T^{\text{jet}}$  is the scalar sum of the transverse momenta of all tau leptons, muons and jets in the event. This variable exploits the fact that signals with large bottom-squark masses are expected to produce highly-boosted particles in the final state.

The transverse mass variable [96, 97], denoted  $m_{T2}$ , is used to discriminate the signal process from the top-quark production background. It is designed to have an endpoint for background processes like top-quark production where the two tau leptons originate from separate decay branches. For the signal process, the two tau leptons originate from a resonant Higgs-boson decay, and the  $m_{T2}$  spectrum has a pronounced tail towards larger values. The  $m_{T2}$  variable is computed as

$$m_{T2} = \min_{\vec{p}_T^a + \vec{p}_T^b = \vec{p}_T^{\text{miss}}} \left( \max \left[ m_T(\vec{p}_T^{\tau_1}, \vec{p}_T^a), m_T(\vec{p}_T^{\tau_2}, \vec{p}_T^b) \right] \right), \quad (1)$$

where  $\vec{p}_T^{\tau_1, \tau_2}$  correspond to the transverse momenta of the two leading tau leptons, and  $(a, b)$  refers to two invisible particles assumed to be produced with transverse momentum  $\vec{p}_T^{a, b}$ . The masses of the invisible particles are free parameters and set to  $m_a = m_b \equiv m_{\text{inv}}$ . The transverse mass  $m_T$  is defined as  $m_T^2(\vec{p}_T^\tau, \vec{p}_T^{\text{inv}}) = m_{\text{inv}}^2 + 2(p_T^\tau \sqrt{m_{\text{inv}}^2 + p_T^{\text{inv}}^2} - \vec{p}_T^\tau \cdot \vec{p}_T^{\text{inv}})$ , where the tau-lepton mass is set to 0 GeV. The  $m_{T2}$  distribution peaks at 0 GeV for both the bottom-squark signal and the dominant  $t\bar{t}$  background when setting  $m_{\text{inv}}$  to 0 GeV, providing poor discrimination. The discrimination improves as  $m_{\text{inv}}$  is increased, and a value of 120 GeV is found to result in an  $m_{T2}$  distribution that best separates the signal from the background. All SRs require  $m_{T2} > 140 \text{ GeV}$ . Some of the CRs also make use of the transverse mass of a tau lepton, which is computed as  $(m_T^\tau)^2 = 2(p_T^\tau E_T^{\text{miss}} - \vec{p}_T^\tau \cdot \vec{p}_T^{\text{miss}})$ .

The last discriminant is  $\text{min}_\Theta$ , defined as the minimal three-dimensional angle of the four combinations between either of the two leading tau leptons and either of the two leading  $b$ -jets. For the  $t\bar{t}$  background, the minimal angle is expected from configurations where the  $b$ -jet and the tau lepton originate from the same top-quark decay, resulting in relatively low values of  $\text{min}_\Theta$ . For  $Z(\tau\tau) + b\bar{b}$  events with a highly-boosted  $Z$  boson, the pair of tau leptons recoils against the  $b$ -jets, and large values of  $\text{min}_\Theta$  are expected. For signal events where  $\tilde{b} \rightarrow b\tilde{\chi}_2^0 \rightarrow bh(\tau\tau)\tilde{\chi}_1^0$ , the angle between the  $b$ -jet and the tau-lepton pair increases with the  $\tilde{b}$  mass, and so does  $\text{min}_\Theta$ . A multi-bin SR with three  $\text{min}_\Theta$  bins ( $< 0.5, [0.5, 1.0], > 1.0$ ) is defined to take advantage of these features. A single-bin SR requiring  $\text{min}_\Theta > 0.6$  is also defined. The product of kinematic acceptance and reconstruction and identification efficiencies of the single-bin SR for the signal process ranges between  $6.4 \cdot 10^{-6}$  at  $m(\tilde{b}) = 250 \text{ GeV}$  and  $m(\tilde{\chi}_2^0) = 150 \text{ GeV}$  and  $1.4 \cdot 10^{-3}$  at  $m(\tilde{b}) = 900 \text{ GeV}$  and  $m(\tilde{\chi}_2^0) = 150 \text{ GeV}$ .

Examples of signal and background kinematic distributions are shown in Figure 2. The two plots show the  $H_T$  and  $m(\tau_1, \tau_2)$  variables after the preselection. The estimated SM background is scaled by the normalization factors from the background fit described in Section 6, and the distributions for several signal models are overlaid.

Table 2: Definition of the single-bin and multi-bin signal regions. The requirements are applied in addition to the preselection from Table 1. The single-bin and multi-bin SRs only differ by the  $\min_{\Theta}$  requirement.

Common SR requirements	
$N_{\mu}$	0
$N_{\tau}$	$\geq 2$
$OS(\tau_1, \tau_2)$	yes
$m(\tau_1, \tau_2)$	[55, 120] GeV
$m_{T2}$	$> 140$ GeV
$H_T$	$> 1100$ GeV
Single-bin SR	
$\min_{\Theta}$	$> 0.6$
Multi-bin SR	
	3 bins: $< 0.5$ , [0.5, 1.0], $> 1.0$

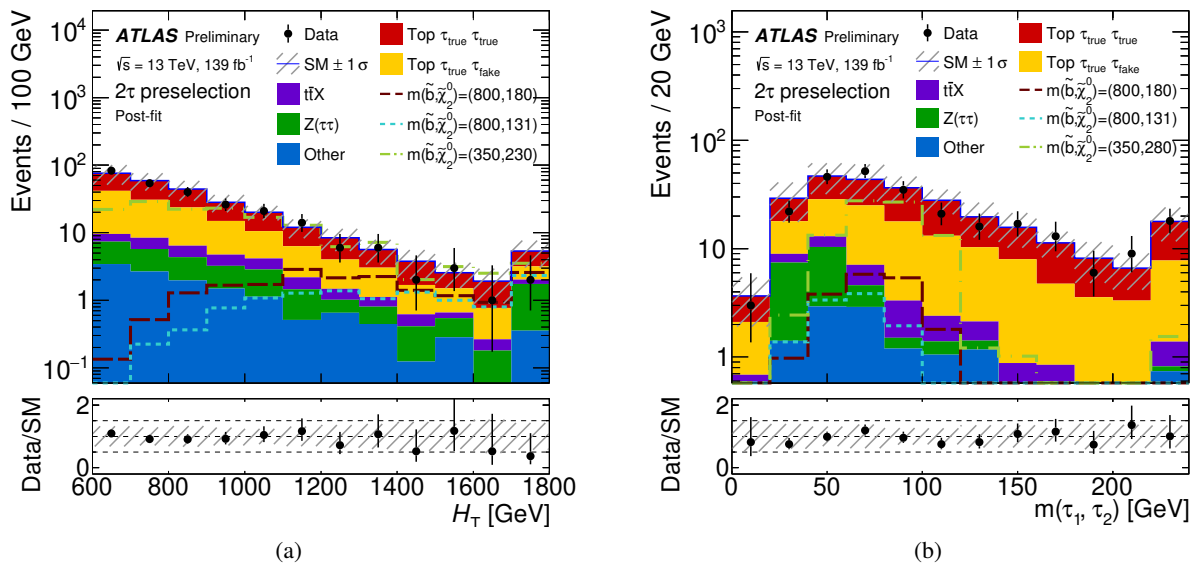


Figure 2: Kinematic distributions of data and SM background for events that pass the preselection and have at least two hadronically decaying tau leptons. Predictions from three signal models are also shown, where the masses  $m(\tilde{b})$  and  $m(\tilde{\chi}_2^0)$  are given in GeV in the legend. Distributions are displayed for the (a)  $H_T$  and (b)  $m(\tau_1, \tau_2)$  variables. The hatched band indicates the total statistical and systematic uncertainties in the SM background. The “other” contribution includes all the backgrounds not explicitly listed in the legend ( $V+jets$  except  $Z(\tau\tau)+jets$ , di-/triboson, multijet). The top-quark and  $Z(\tau\tau)$  background contributions are scaled with the normalization factors obtained from the background-only fit described in Section 6. The rightmost bin includes the overflow.

## 6 Background estimation

The largest backgrounds in the SRs are  $t\bar{t}$  and single-top-quark processes, referred to as top-quark background, and  $Z(\tau\tau)$  produced in association with  $b$ -jets. Subdominant contributions arise from  $t\bar{t}X$  processes, while other backgrounds such as multijet or di- and triboson production are found to be negligible. The normalization of the two dominant backgrounds is fitted to the data in dedicated control regions (CRs) kinematically close to the SRs but where little signal is expected. The normalization factors are derived with

a likelihood fit based on the HistFITTER framework [98]. The fit uses as input the observed data yields, the expected yields predicted from simulation, as well as the statistical and systematic uncertainties described in Section 7. Two main fit setups are employed in the analysis. The background-only fit refers to the configuration that only includes the CRs, and where no signal is considered. The signal-plus-background fit includes both the CRs and the SRs, and it takes into account a possible signal contribution in the fitted regions. It is used to establish exclusion limits as discussed in Section 8. In both cases, the fit is performed simultaneously over all the relevant regions. Subdominant background contributions are normalized according to their cross sections and the integrated luminosity of the data. The multijet background is determined from data. Validation regions (VRs) are defined in phase-space regions as close as possible to that of the SRs. The VRs are not included in the fit. They are used to validate the background model extrapolation from the CRs to the SRs by comparing the observed data with the fitted background predictions. As such, they are designed to have little signal contribution. The methods to estimate the various backgrounds are described in the following, together with the associated CRs and VRs.

Multijet production is an important background at hadron colliders, but it is efficiently suppressed in this analysis by the requirement of two hadronically decaying tau leptons, two  $b$ -jets, large  $E_T^{\text{miss}}$ , and  $\Delta\phi(\text{jet}_{1,2}, \vec{p}_T^{\text{miss}}) > 0.5$ . A data-driven jet-smearing method [99] is employed to estimate this background. Events recorded by single-jet triggers are processed through an energy smearing procedure that emulates  $E_T^{\text{miss}}$  originating from resolution effects. The normalization of the smeared pseudo-data template is derived in events where one of the two leading jets is aligned with  $\vec{p}_T^{\text{miss}}$  in the transverse plane. Except for that multijet-enriched selection, the multijet background is found to be negligible in all analysis selections. Therefore, its normalization is kept constant in the fits, for simplicity.

The design of the control regions for the top-quark and  $Z(\tau\tau) + b\bar{b}$  backgrounds is driven by two main considerations. Firstly, the hadronically decaying tau leptons selected in the analysis are either prompt tau leptons from electroweak boson decays, or jets misidentified as tau leptons. They are referred to as *true* tau leptons ( $\tau_{\text{true}}$ ) and *fake* tau leptons ( $\tau_{\text{fake}}$ ), respectively, and their contributions must be handled separately in the background model. No such distinction is made for  $b$ -jets, as the fraction of misidentified  $b$ -jets does not exceed 10% in the analysis phase space. The top-quark background in the SRs is composed of  $\tau_{\text{true}}\tau_{\text{true}}$  and  $\tau_{\text{true}}\tau_{\text{fake}}$  contributions of comparable magnitude, where one tau lepton comes from a  $W$ -boson decay, and the second tau lepton either comes from the other  $W$ -boson decay or from a jet misidentified as a tau lepton. The  $\tau_{\text{fake}}\tau_{\text{fake}}$  contribution is negligible due to the large jet rejection provided by the tau-lepton identification algorithm. In the case of  $Z(\tau\tau) + b\bar{b}$  events, only the  $\tau_{\text{true}}\tau_{\text{true}}$  contribution is found to be relevant. Secondly, the background normalization factors cannot be accurately determined using events containing two hadronically decaying tau leptons and two  $b$ -jets, as the low event yields remaining after the preselection do not allow to define control regions with sufficient statistical power, high purity, and low signal contamination.

Because of these limitations the CRs are based on final states where either one or two tau leptons are replaced with muons. The CR\_Top\_μ $\tau_{\text{true}}$  and CR\_Top\_μ $\tau_{\text{fake}}$  selections are defined to respectively target top-quark events with one muon plus either one  $\tau_{\text{true}}$  or one  $\tau_{\text{fake}}$  in the final state, where the muon replaces a  $\tau_{\text{true}}$  from one of the  $W$ -boson decays. The CR\_Z\_μμ2b region is defined to select  $Z(\mu\mu) + b\bar{b}$  events. By trading  $W(\tau\nu)$  for  $W(\mu\nu)$  and  $Z(\tau\tau)$  for  $Z(\mu\mu)$ , the CRs target the desired background processes but benefit from larger yields due to the branching ratio  $\mathcal{B}(\tau \rightarrow \tau_{\text{had}}\nu_\tau)$  of 65% that does not apply to muons, and to the reconstruction and identification efficiencies that are higher for muons. In the top-quark CRs, event yields are further increased by a combinatorial factor of two.

The normalization factors derived for background events with muons are not directly applicable to background events in the SRs that contain two hadronically decaying tau leptons. The replacement of

Table 3: Definition of the control regions used for the top-quark background. The requirements are applied in addition to the preselection. A dash means that no requirement on this variable is applied.

	CR_Top_μ	CR_Top_τ <sub>true</sub>	CR_Top_μτ <sub>true</sub>	CR_Top_μτ <sub>fake</sub>
$N_\mu$	1	0	1	1
$N_\tau$	0	1	1	1
OS( $\mu, \tau$ )	–	–	yes	yes
$H_T$			[600, 1000] GeV	
$m_T^\tau$	–	< 80 GeV	< 80 GeV	> 100 GeV

tau leptons with muons has an impact on the reconstructed event kinematics and the selection efficiency of background processes, which needs to be accounted for. This is done by introducing additional CRs and normalization factors, two for the top-quark background and two for the  $Z(\tau\tau) + b\bar{b}$  background, that allow to extrapolate from muon to tau-lepton selections. As mentioned in Section 4, corrections are already applied to muons and tau leptons in the simulation to match the efficiencies and energy calibration measured in data. The background normalization factors from the additional CRs thus mostly account for acceptance effects and are related to the accuracy of MC event generators.

The definition of the four control regions used to normalize the top-quark background are summarized in Table 3. The CR\_Top\_μτ<sub>true</sub> and CR\_Top\_μτ<sub>fake</sub> regions select events that contain exactly one muon and one tau lepton of opposite electric charge. Like all control regions defined in this analysis, they use the  $H_T$  range from 600 to 1000 GeV. For CR\_Top\_μτ<sub>true</sub>, the tau-lepton transverse mass  $m_T^\tau$  must be lower than 80 GeV, which results in a high purity of true tau leptons. For CR\_Top\_μτ<sub>fake</sub>,  $m_T^\tau$  has to be larger than 100 GeV, which gives a roughly equal mix of true and fake tau leptons. The CR\_Top\_τ<sub>true</sub> selection is identical to that of CR\_Top\_μτ<sub>true</sub> except that events must not contain a muon. This region has a high purity in top-quark background events decaying semileptonically with a true tau lepton in the final state. The CR\_Top\_μ selection is defined in a similar way, with one muon and no tau lepton, selecting high-purity semileptonic top-quark processes with a muon in the final state.

The way the four CRs from Table 3 are used to derive normalization factors for the top-quark background processes is illustrated in Figure 3(a). The expected yields for top-quark production with true and fake tau leptons from Monte Carlo simulation are respectively multiplied by normalization factors  $\omega_{\text{true tau}}$  and  $\omega_{\text{fake tau}}$ , that are free-floating in the fit and constrained from data predominantly through CR\_Top\_μτ<sub>true</sub> and CR\_Top\_μτ<sub>fake</sub>. To account for the different flavor of the lepton in the signal region (with two tau leptons) and the control region (one tau lepton and one muon), the top-quark production yields are further multiplied by additional free-floating normalization factors  $\omega_{1\text{tau}}$  and  $\omega_{1\text{mu}}$ , which are constrained predominantly through the regions CR\_Top\_τ<sub>true</sub> and CR\_Top\_μ. The ratio  $\text{TF}_{\text{Top}} \equiv \omega_{1\text{tau}}/\omega_{1\text{mu}}$  is used to correct the difference between requiring a muon and a true tau lepton. This means that a simulated top-quark event with one true and one fake tau lepton in one of the signal regions receives a normalization factor  $\omega_{\text{fake tau}} \times \text{TF}_{\text{Top}}$ , and a simulated top-quark event with two true tau leptons a normalization factor  $\omega_{\text{true tau}} \times \text{TF}_{\text{Top}}$ .

Figure 4 shows several examples of distributions from the four control regions associated with the top-quark background. In these plots, the predicted background contributions from simulation are scaled with the normalization factors obtained from the background-only fit. All of the CRs show good agreement between the SM prediction and the data. They also have high purity in the respective top-quark background

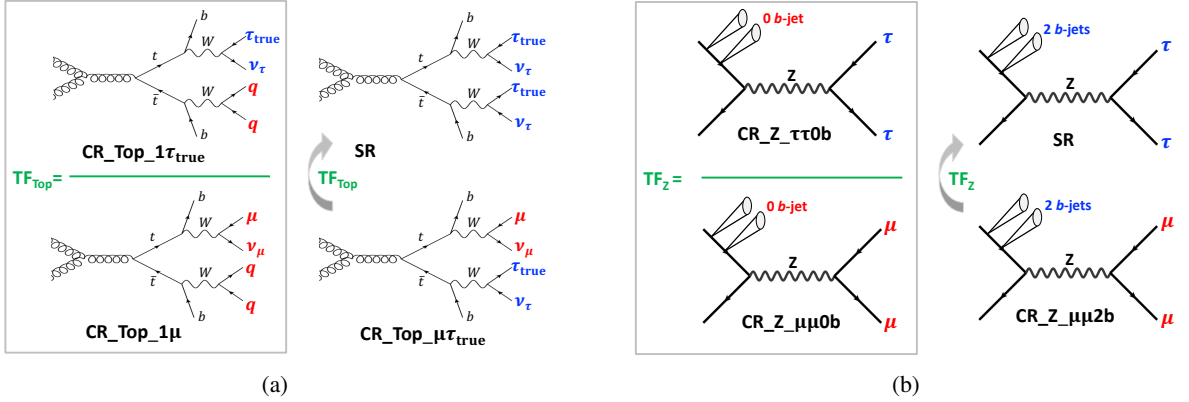


Figure 3: Schematic representation of the control region setup that is used to constrain the normalization of the (a) top-quark and (b)  $Z(\tau\tau)$ +jets backgrounds in the signal regions. The arrows represent the transfer factors associated with the replacement of muons with true tau leptons, which correct for acceptance. For the top-quark background, the sketch illustrates the normalization strategy for the  $\tau_{\text{true}}$   $\tau_{\text{true}}$  contribution. A similar strategy is employed for the  $\tau_{\text{true}}$   $\tau_{\text{fake}}$  contribution, where the  $\tau_{\text{fake}}$  can originate from a jet from a hadronically decaying  $W$  boson, a  $b$ -jet, or a jet from initial-state radiation.

Table 4: Definition of the control regions used for the  $Z$ +jets background. The requirements are applied in addition to the set of preselection criteria reported in the upper part of Table 1. A dash means that no requirement on this variable is applied.

	CR_Z_mu2b	CR_Z_mu0b	CR_Z_tau0b
Trigger	single-muon		$E_{\text{T}}^{\text{miss}}$
$N_{\mu}$	2		0
$N_{\tau}$	0		2
$N_{b\text{-jets}}$	2	0	0
$p_{\text{T}}(\mu_1)$	$> 30 \text{ GeV}$		–
$E_{\text{T}}^{\text{miss}}$	$< 100 \text{ GeV}$		$> 200 \text{ GeV}$
$p_{\text{T}}(\mu_1, \mu_2)$	$> 200 \text{ GeV}$		–
$m(\mu_1, \mu_2)$	$[81, 101] \text{ GeV}$		–
$m_{\text{T}}^{\tau_1} + m_{\text{T}}^{\tau_2}$	–		$< 100 \text{ GeV}$
$H_{\text{T}}$		$[600, 1000] \text{ GeV}$	

processes except for CR\_Top\_mu\_tau\_fake, where the purity is only 43% because it is difficult to isolate the contribution of the top-quark background with fake tau leptons.

The three control regions that target the  $Z(\tau\tau)$  background are summarized in Table 4. The CR\_Z\_mu2b selection is defined using events with two muons of opposite electric charge, taken as proxies for two true tau leptons, and two  $b$ -jets. Since  $Z(\mu\mu)$ +jets processes do not have large  $E_{\text{T}}^{\text{miss}}$  in the final state, the events are selected using a single-muon trigger, which reaches its efficiency plateau for  $p_{\text{T}}(\mu) > 30 \text{ GeV}$ . The invariant mass of the di-muon system is required to be within 10 GeV of the  $Z$ -boson mass, and  $E_{\text{T}}^{\text{miss}}$  to be lower than 100 GeV to increase the purity of the selection. To move the CR closer to the relevant phase space,  $H_{\text{T}}$  must be in the range  $[600, 1000] \text{ GeV}$ , and the transverse momentum of the muon pair  $p_{\text{T}}(\mu_1, \mu_2)$  must be larger than 200 GeV, which is a typical value found in simulation for the  $p_{\text{T}}$  of the  $Z$  boson in

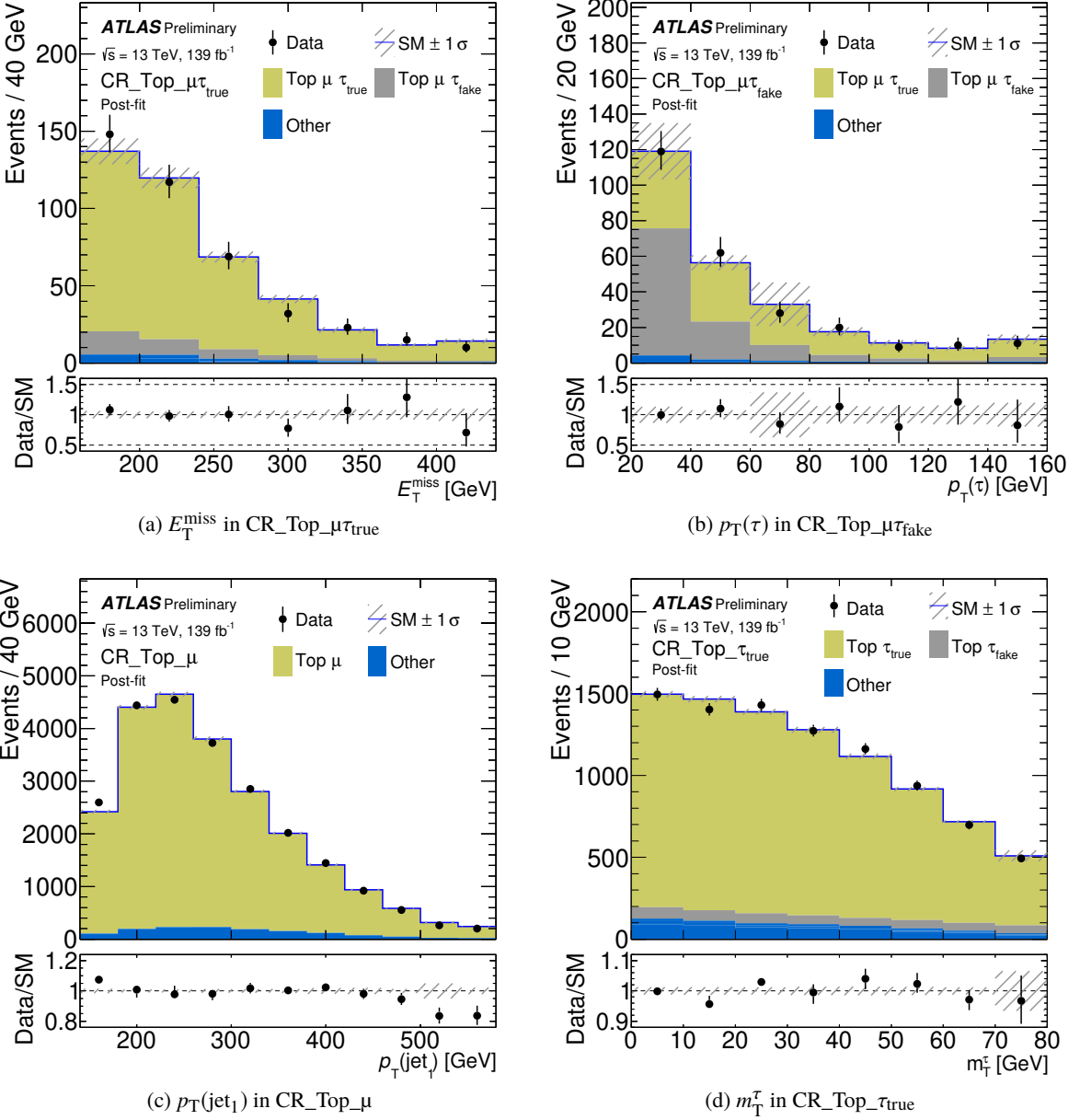


Figure 4: Kinematic distributions from the four control regions associated with the top-quark background, showing (a)  $E_T^{\text{miss}}$  in CR\_Top\_μτ<sub>true</sub>, (b)  $p_T(\tau)$  in CR\_Top\_μτ<sub>fake</sub>, (c)  $p_T(\text{jet}_1)$  in CR\_Top\_μ, and (d)  $m_T^{\tau}$  in CR\_Top\_τ<sub>true</sub>. The hatched band indicates the total statistical and systematic uncertainties in the SM background. The top-quark and  $Z(\tau\tau)$  background contributions are scaled with the normalization factors obtained from the background-only fit. The “other” contribution includes all the backgrounds not explicitly listed in the legend ( $V+\text{jets}$ ,  $t\bar{t}X$ , di-/triboson, multijet). The rightmost bin includes the overflow.

$Z(\tau\tau)$  events after the preselection. The  $Z(\mu\mu)$  background is multiplied by the free-floating normalization factor  $\omega_{Z\mu\mu 2b}$ , which is constrained through CR\_Z\_μμ2b.

The two additional control regions CR\_Z\_μμ0b and CR\_Z\_ττ0b are used to correct for the difference in acceptance and efficiency when replacing the tau leptons with muons to estimate the  $Z+\text{jets}$  background.

Table 5: Values of normalization and transfer factors obtained from the background-only fit, in the top part of the table for top-quark background processes, in the bottom part for  $Z$ +jets. The control regions that are primarily affecting the normalization factors are listed, together with the purity of the CR in the relevant background process. As  $TF_{Top}$  and  $TF_Z$  are ratios of two normalization factors, one of which (the denominator) is listed in the row directly above, the table lists the respective second control region (the numerator of the ratio) and its purity in top-quark or  $Z(\tau\tau) + b\bar{b}$  events.

Normalization / transfer factor	Fitted value	Control region	Purity
$\omega_{\text{true tau}}$	$0.88 \pm 0.16$	CR_Top_μτ <sub>true</sub>	86%
		CR_Top_μτ <sub>fake</sub>	53%
$\omega_{\text{fake tau}}$	$0.79 \pm 0.30$	CR_Top_μτ <sub>fake</sub>	43%
		CR_Top_μτ <sub>true</sub>	9%
$\omega_{1\mu}$	$0.91 \pm 0.10$	CR_Top_μ	94%
$TF_{Top} \equiv \omega_{1\text{tau}}/\omega_{1\mu}$	$0.98 \pm 0.04$	CR_Top_τ <sub>true</sub>	88%
$\omega_{Z\mu\mu 2b}$	$1.28 \pm 0.12$	CR_Z_μμ2b	89%
$\omega_{Z\mu\mu 0b}$	$1.00 \pm 0.05$	CR_Z_μμ0b	96%
$TF_Z \equiv \omega_{Z\tau\tau 0b}/\omega_{Z\mu\mu 0b}$	$0.99 \pm 0.17$	CR_Z_ττ0b	79%

The interplay of these CRs is illustrated in Figure 3(b). The CR\_Z\_μμ0b selection is the same as CR\_Z\_μμ2b but with a  $b$ -jet veto, whereas CR\_Z\_ττ0b requires the presence of two tau leptons with opposite electric charge and no  $b$ -jet. The CR\_Z\_ττ0b events are selected with a  $E_T^{\text{miss}}$  trigger and  $E_T^{\text{miss}} > 200 \text{ GeV}$  as is done for the SRs, and muons are vetoed in this region. Additionally, the sum of tau transverse masses  $m_T^{\tau_1} + m_T^{\tau_2}$  has to be lower than 100 GeV to increase the purity in  $Z(\tau\tau)$  events. In all of these three CRs,  $H_T$  is again required to be within [600, 1000] GeV.

From these two auxiliary control regions, the free-floating normalization factor  $\omega_{Z\mu\mu 0b}$  and transfer factor  $TF_Z$  are derived in the background fit. The background normalization in CR\_Z\_μμ0b is absorbed in  $\omega_{Z\mu\mu 0b}$ .  $TF_Z$  transfers the normalization from CR\_Z\_μμ0b to CR\_Z\_ττ0b,  $TF_Z \equiv \omega_{Z\tau\tau 0b}/\omega_{Z\mu\mu 0b}$ , and from CR\_Z\_μμ2b to the SRs, i.e.  $Z(\tau\tau) + b\bar{b}$  events in the SRs are scaled by  $\omega_{Z\mu\mu 2b} \cdot TF_Z$ .

All normalization and transfer factors are obtained from a simultaneous fit of the seven CRs for the top-quark and  $Z(\tau\tau)$  backgrounds. Table 5 lists the values of the normalization factors and transfer factors and their uncertainties, the name of the control regions that are used to constrain the normalization factors and the respective purities of the control regions in top-quark or  $Z$ +jets events. The transfer factors  $TF_{Top}$  and  $TF_Z$  are computed from ratios of two normalization factors as explained above. For these, one row in the table ( $\omega_{1\mu}$  and  $\omega_{Z\mu\mu 0b}$ ) gives the values forming the respective denominators of the ratio, showing the agreement of data and simulated events in these regions. The rows below that give the transfer factors ( $TF_{Top}$  and  $TF_Z$ ). In these rows, the table lists the second control region (the numerator of the ratio) and its purity.

Three validation regions are defined to check the extrapolation from CR\_Top\_μτ<sub>true</sub>, CR\_Top\_μτ<sub>fake</sub>, and CR\_Z\_μμ2b in the  $H_T$  variable. This is done by changing the requirement on  $H_T$  that is applied in the CRs from  $600 \text{ GeV} < H_T < 1000 \text{ GeV}$  to  $1000 \text{ GeV} < H_T < 1500 \text{ GeV}$  in the VRs, while keeping all other requirements the same as for the respective CRs. Shifting the  $H_T$  range moves the validation regions closer to the signal regions, which require  $H_T > 1100 \text{ GeV}$ . The VRs and the SRs are mutually exclusive due to the muon veto that is part of the signal-region selections. The names of the three VRs match the ones of the corresponding CRs. A fourth validation region, VR\_Top\_ττ, is defined to validate the extrapolation

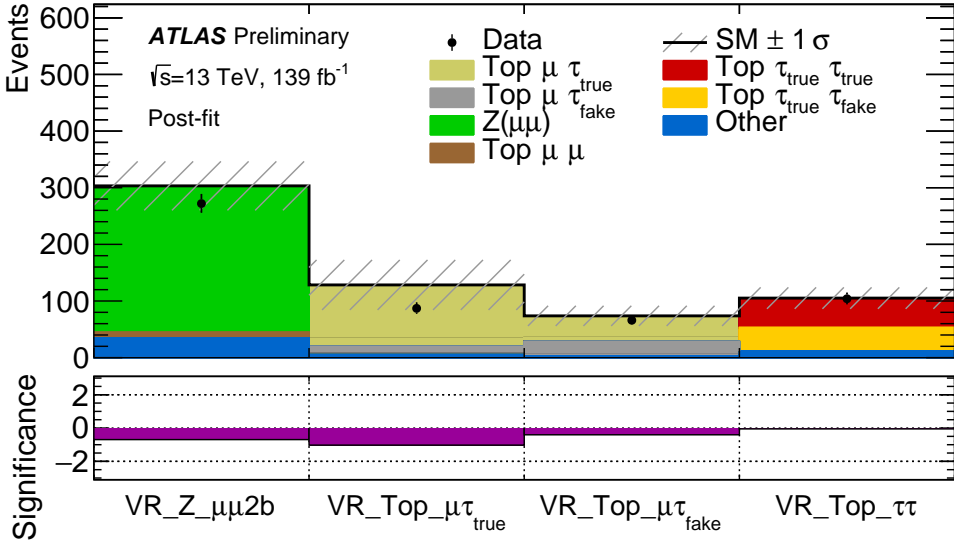


Figure 5: The upper panel shows the expected number of SM background events and the number of events observed in data for each of the four validation regions. In the lower panel, the significance of the deviation of the observed yield from the expected yield is shown. The top-quark,  $Z(\tau\tau)$  and  $Z(\mu\mu)$  background contributions are scaled with the normalization factors obtained from the background-only fit described in Section 6. The hatched band indicates the total statistical and systematic uncertainties in the SM background. The “other” contribution includes all the backgrounds not explicitly listed in the legend ( $V+jets$  except  $Z(\mu\mu)+jets$ ,  $t\bar{t}X$ , di-/triboson, multijet).

from muons to tau leptons in events with two  $b$ -jets and two hadronically decaying tau leptons which pass the  $E_T^{\text{miss}}$  trigger or the  $E_T^{\text{miss}} + b$ -jet trigger and the corresponding trigger-plateau requirements. To avoid overlap of this VR with the SRs,  $H_T$  is required to be within  $[600, 1000]$  GeV. In addition, the visible di-tau mass  $m(\tau_1, \tau_2)$  is required to be either lower than 40 GeV or larger than 90 GeV to reduce the contribution from a possible bottom-squark signal.

Figure 5 shows that the expected background yields after the fit and the observed yields agree within one standard deviation for all four validation regions, demonstrating a good modeling of the SM background. Figure 6 shows the  $\min\Theta$  distribution in  $VR_{\text{Top}}\tau\tau$ . Good agreement between the background model and the data is observed. The contribution of a potential signal from the model in Figure 1 to the control regions does not exceed 7% at the low end of the range of bottom-squark masses covered by the signal models and quickly falls to below a percent at the high end. For the validation regions it is around 15% for low  $m(\tilde{b})$  and again falls to a percent or less for larger  $m(\tilde{b})$ .

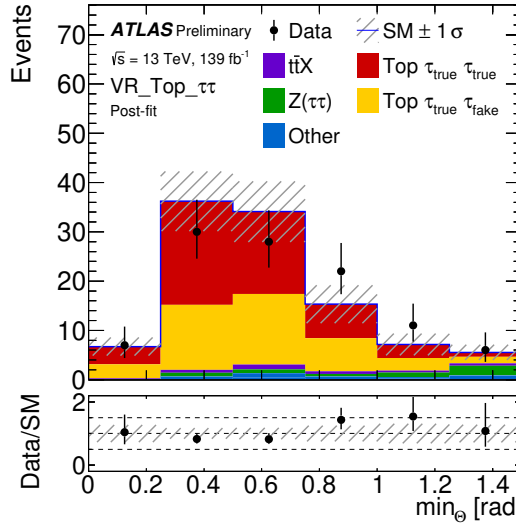


Figure 6: Kinematic distribution of the  $\min_{\theta}$  variable in the VR\_Top\_ $\tau\tau$  region. The hatched band indicates the total statistical and systematic uncertainties in the SM background. The “other” contribution includes all the backgrounds not explicitly listed in the legend ( $V+jets$  except  $Z(\tau\tau)+jets$ , di-/triboson, multijet). The top-quark and  $Z(\tau\tau)$  background contributions are scaled with the normalization factors obtained from the background-only fit. The rightmost bin includes the overflow.

## 7 Systematic uncertainties

The experimental uncertainties considered in this analysis comprise systematic uncertainties in the reconstruction, identification, calibration and corrections applied to the physical objects used in the analysis. They are assumed to be correlated across analysis regions and between the background processes and the signal. Theoretical uncertainties include contributions from generator modeling as well as cross-section uncertainties. They are assumed to be correlated across analysis regions but uncorrelated between different background processes. When assuming no correlation between analysis regions, the total background uncertainty increases by about 5 percentage points for the single-bin SR, and the exclusion contour does not change significantly.

The experimental uncertainties related to jets include uncertainties in the energy scale [81] and resolution [100], jet-vertex-tagging uncertainties [83] and flavor-tagging uncertainties [84, 101, 102]. Flavor-related uncertainties come from the uncertainties of data-to-simulation correction factors for efficiencies and fake rates and from the extrapolation over jet  $p_T$ . Tau-lepton uncertainties arise from the energy calibration, and reconstruction and identification efficiencies [86, 90]. The energy scale uncertainties include the non-closure of the calibration and uncertainties in the detector response estimated from simulation, as well as uncertainties in the relative calibration of data and simulation measured in  $Z(\tau_{\mu}\tau_{had})$  events. A high- $p_T$  uncertainty based on single-particle response uncertainties is taken into account. Muon-related uncertainties [91] are not relevant in the signal regions, as events with muons do not enter these, but they can be important in control regions with muons. Uncertainties related to electrons have a negligible impact on this analysis. The systematic uncertainties affecting the energy or momentum of calibrated objects are propagated to the  $E_T^{\text{miss}}$  calculation. Specific uncertainties in the soft-term contribution to the  $E_T^{\text{miss}}$  [93] are also considered.

The theoretical uncertainties related to variations of the PDFs [76], strong coupling constant  $\alpha_s$  and

Table 6: Dominant systematic uncertainties in the background prediction for the signal regions after the fit to the control regions. ‘‘Other’’ includes the uncertainties arising from muons, jet-vertex tagging, modeling of pile-up, the  $E_T^{\text{miss}}$  computation, multijet background, and luminosity. The individual uncertainties can be correlated and do not necessarily add up quadratically to the total uncertainty.

Uncertainty	Single-bin SR	Multi-bin SR		
		$\min\Theta < 0.5$	$0.5 < \min\Theta < 1.0$	$\min\Theta > 1.0$
Generator modeling	37%	42%	44%	27%
Normalization / transfer factors	15%	11%	12%	18%
JER and JES	12%	5.1%	9.8%	22%
Tau leptons	8.3%	3.5%	2.3%	15%
MC statistical uncertainty	6.9%	6.8%	7.2%	11%
Flavor tagging	3.8%	1.0%	1.8%	5.4%
Other	2.9%	1.3%	1.8%	6.6%
Total	40%	43%	46%	41%

renormalization and factorization scales  $\mu_r$  and  $\mu_f$  [103] are evaluated from generator weights for all background samples. The sets include the nominal PDF as well as 100 variations. The PDF uncertainty is obtained as the envelope of all the variations. The uncertainty related to  $\alpha_s$  is evaluated by computing  $\alpha_s = 0.119$  and  $\alpha_s = 0.117$  parametrizations and averaging the difference between them. The PDF and  $\alpha_s$  uncertainties are then added quadratically. In order to derive the scale uncertainties,  $\mu_r$  and  $\mu_f$  are varied up and down by a factor of two. Three independent nuisance parameters are used, two resulting from keeping one of the scales constant while varying the other one, and the third being the coherent variation of both scales. The variations are normalized to the nominal sum of weights so that the effect on the normalization included in the cross-section uncertainty is not double-counted. For all simulated processes that are not normalized to the data, uncertainties in the cross section and in the integrated luminosity of the data are applied.

For  $t\bar{t}$  and single-top-quark production, generator uncertainties related to hard scattering and matching are evaluated by comparing PowhegBox+Pythia with MadGraph5\_aMC@NLO+Pythia. Parton-showering uncertainties are estimated by comparing to PowhegBox+Herwig7. Uncertainties in the initial-state and final-state radiation are evaluated by simultaneously testing the impact of scale variations and eigenvariations of the A14 tune [45]. For  $t\bar{t}$  production, an additional comparison with the  $h_{\text{damp}}$  parameter set to  $3m_{\text{top}}$  is included. For single-top-quark production, an uncertainty in the treatment of the  $Wt/t\bar{t}$  interference is considered by comparing samples produced with the nominal diagram-removal scheme [104] with alternative samples generated with a diagram-subtraction scheme [43, 104].

For the  $V+\text{jets}$  processes, additional uncertainties related to the resummation and CKKW matching scales [63, 64] are considered. For the  $Z(\mu\mu)+\text{jets}$  and  $Z(\tau\tau)+\text{jets}$  backgrounds, a comparison of the nominal Sherpa samples with alternative samples produced with MadGraph5\_aMC@NLO+Pythia is done. For diboson and  $t\bar{t}X$  samples, the PDF, scale and cross-section uncertainties are used.

For the bottom-squark signal samples, uncertainties in the acceptance related to the factorization and renormalization scales, merging scales, parton shower tuning and radiation uncertainties are considered. An additional uncertainty accounts for differences between samples produced with the full detector simulation and the parametrized calorimeter response.

Table 7: The observed event yields in data, the total expected yields from SM processes obtained from the background-only fit and breakdown of individual contributions, and the expected signal contributions for two benchmark models are shown for the single-bin and the three bins of the multi-bin signal regions. Total uncertainties combining the statistical and systematic uncertainties are quoted for the background processes. For the signal, the quoted uncertainties are only statistical. The row “other” combines all SM background contributions that are not listed explicitly, covering  $V$ +jets except for  $Z(\tau\tau)$ +jets, multijet, diboson and triboson contributions. The dash means that no events pass the selection.

	Single-bin SR		Multi-bin SR	
	$\min_\Theta < 0.5$	$0.5 < \min_\Theta < 1.0$	$\min_\Theta > 1.0$	
Observed events	4	3	1	3
Total SM background	$3.8 \pm 1.5$	$2.7 \pm 1.1$	$3.5 \pm 1.6$	$1.5 \pm 0.6$
top quark $\tau_{\text{true}} \tau_{\text{true}}$	$1.4 \pm 0.9$	$1.6 \pm 0.7$	$1.9 \pm 1.0$	$0.30^{+0.41}_{-0.30}$
top quark $\tau_{\text{true}} \tau_{\text{fake}}$	$0.92 \pm 0.62$	$0.76 \pm 0.43$	$0.96 \pm 0.69$	$0.22 \pm 0.17$
top quark $\tau_{\text{fake}} \tau_{\text{fake}}$	$0.11^{+0.26}_{-0.11}$	$0.06 \pm 0.06$	$0.12^{+0.23}_{-0.12}$	$0.04^{+0.05}_{-0.04}$
$t\bar{t}X$	$0.52 \pm 0.42$	$0.18 \pm 0.10$	$0.26^{+0.31}_{-0.26}$	$0.31 \pm 0.22$
$Z(\tau\tau)$ +jets	$0.73 \pm 0.25$	$0.05 \pm 0.05$	$0.17 \pm 0.16$	$0.59 \pm 0.22$
other	$0.07 \pm 0.04$	—	$0.04 \pm 0.01$	$0.06 \pm 0.03$
$m(\tilde{b}, \tilde{\chi}_2^0) = (800, 131) \text{ GeV}$	$5.6 \pm 1.4$	$0.14 \pm 0.06$	$1.5 \pm 0.4$	$4.3 \pm 1.1$
$m(\tilde{b}, \tilde{\chi}_2^0) = (800, 180) \text{ GeV}$	$9.3 \pm 2.2$	$0.08^{+0.14}_{-0.08}$	$2.4 \pm 0.6$	$7.1 \pm 1.7$

A summary of the dominant systematic uncertainties in the background prediction for the signal regions is given in Table 6. The largest source of uncertainty is the generator modeling, and here in particular the modeling of the top-quark background, mainly the modeling of the hard scatter process and ISR uncertainties. Second-leading in size is the total uncertainty in the normalization and transfer factors, which is obtained from the fit. As the transfer factors are ratios of normalization factors, and a large part of the uncertainties cancel in the ratio, the uncertainties on the transfer factors are comparably small.

## 8 Results

The event yields for all signal regions are reported in Table 7. The SM background prediction is based on the background-only fit described in Section 6. To illustrate the order of magnitude of the contribution of signal events, the expected yields for two benchmark signal models are included in the table. The single-bin SR and the first two bins of the multi-bin SR are dominated by top-quark production, whereas for  $\min_\Theta > 1.0$  the  $Z(\tau\tau)$  background is the largest contribution. Other SM processes contribute very little to the signal regions. Figure 7 shows a comparison of data and background yields in the SRs together with the corresponding significances quantifying the deviation of the observed yields from the SM expectation in the bottom panel. No significant excess of data above the expected yields from the SM background processes is observed in any of the signal regions. The  $p$ -value for the event yield in the single-bin signal region to fluctuate to the observed value under the background-only hypothesis is  $p(s = 0) = 0.44$ .

Exclusion contours at the 95% confidence level (CL) are derived from the yields in the multi-bin signal region for the two-dimensional parameter space of  $m(\tilde{b})$  and  $m(\tilde{\chi}_2^0)$  of the simplified model from Figure 1.

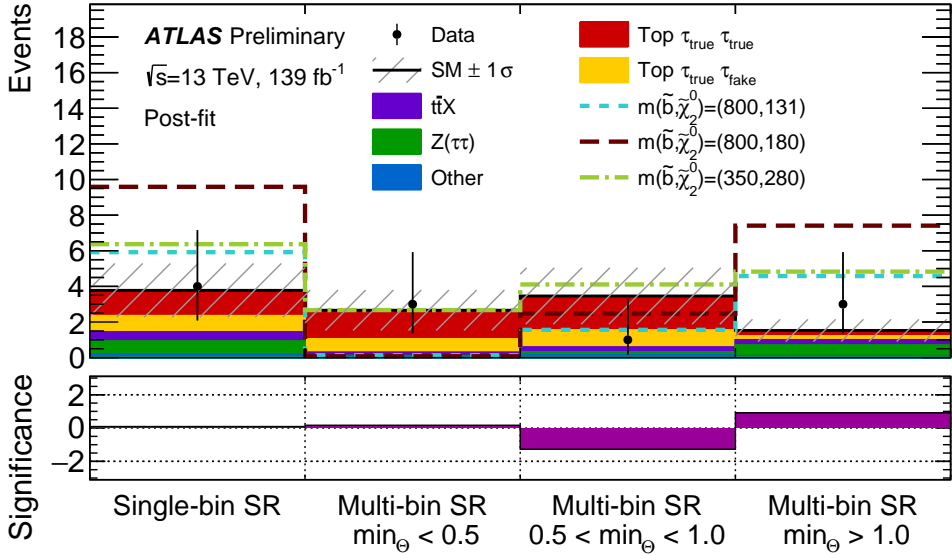


Figure 7: Comparison of the expected and observed event yields in the signal regions defined in Table 2. The top-quark and  $Z(\tau\tau)$  background contributions are scaled with the normalization factors obtained from the background-only fit. The “other” contribution includes all the backgrounds not explicitly listed in the legend ( $V$ +jets except  $Z(\tau\tau)$ +jets, di-/triboson, multijet). The hatched band indicates the total statistical and systematic uncertainties in the SM background. The contributions from three signal models to the signal regions are also displayed, where the masses  $m(\tilde{b})$  and  $m(\tilde{\chi}_2^0)$  are given in GeV in the legend. The lower panel shows the significance of the deviation of the observed yield from the expected background yield.

A fixed mass difference of 130 GeV between the second-lightest neutralino  $\tilde{\chi}_2^0$  and lightest neutralino  $\tilde{\chi}_1^0$  is assumed for all signal models. The compatibility of the data with the background-only and signal-plus-background hypotheses is evaluated using a one-sided profile-likelihood-ratio test statistic and the  $CL_s$  prescription [105]. Systematic uncertainties are treated as nuisance parameters with Gaussian probability densities in the likelihood function. The resulting observed and expected exclusion contours are shown in Figure 8. The uncertainties in the cross section of the supersymmetric signal are not included in the fit but shown as an uncertainty band around the observed limit contour. Due to the observed data being larger than the expected total background in the highest  $\min_\Theta$  bin, which is most sensitive to models with large  $m(\tilde{b})$ , the observed exclusion contour deviates inwards from the expected contour with larger  $m(\tilde{b})$ , but it stays within the uncertainty band of the expected limit. The search is optimized for the low- $m(\tilde{\chi}_2^0)$  region and has sensitivity to models with  $m(\tilde{\chi}_2^0)$  up to 300 GeV. Bottom squarks with masses up to 850 GeV are excluded in this region. For  $m(\tilde{\chi}_2^0)$  below about 200 GeV, the softer  $E_T^{\text{miss}}$  spectrum of the signal results in a lower acceptance, leading to a slightly reduced exclusion reach on the bottom-squark mass. The parameter-space region where  $\Delta m(\tilde{b}, \tilde{\chi}_2^0) \lesssim 20$  GeV cannot be excluded as the bottom-squark decay products are not boosted enough, and the stringent kinematic requirements in the SRs result in low signal acceptance. These results are overlaid onto the observed exclusion contour from a previous ATLAS search [22] to demonstrate the complementarity of the two approaches. The new results have unique sensitivity to a previously uncovered region of parameter space at low  $\tilde{\chi}_2^0$  masses, where the previous search quickly loses sensitivity.

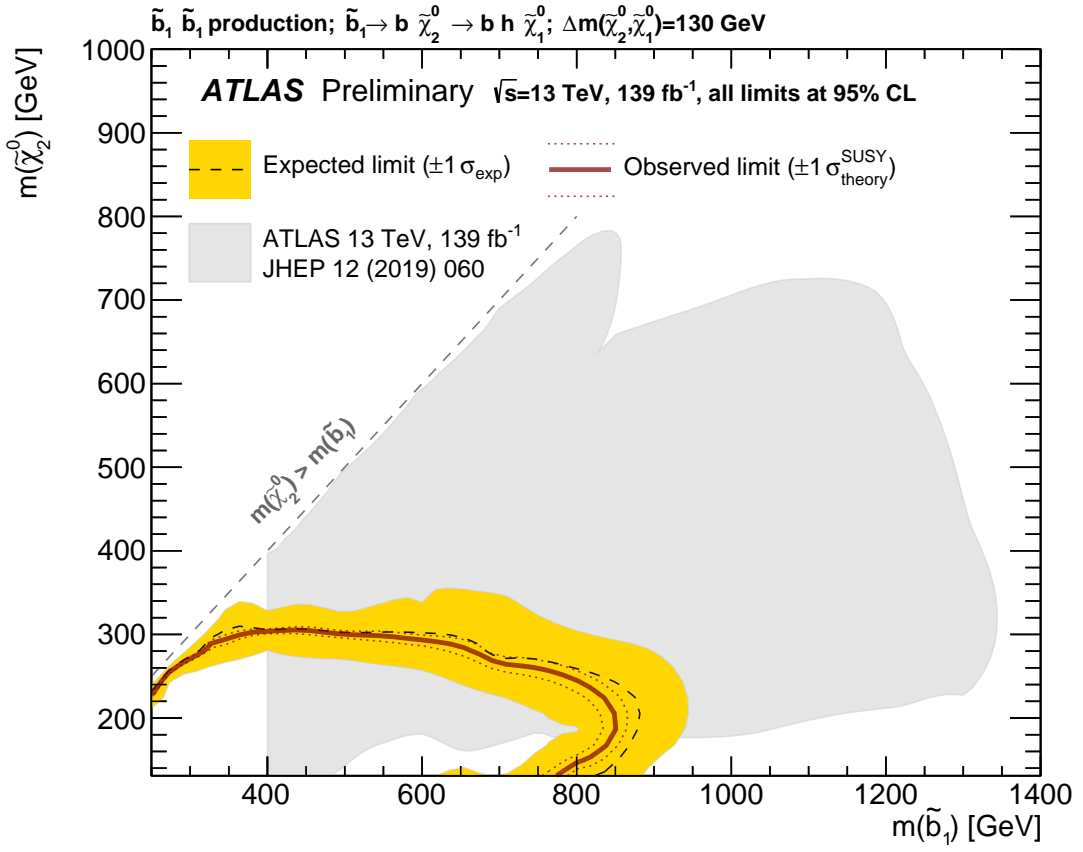


Figure 8: Exclusion contours at the 95% CL as function of  $m(\tilde{b})$  and  $m(\tilde{\chi}_2^0)$ , assuming  $\Delta m(\tilde{\chi}_2^0, \tilde{\chi}_1^0) = 130$  GeV. Observed and expected limits are shown for the present search that requires hadronically decaying tau leptons,  $b$ -jets and  $E_T^{\text{miss}}$  in the final state. The observed exclusion limit from a previous ATLAS search [22] that requires  $b$ -jets and  $E_T^{\text{miss}}$  in the final state is also displayed. The region  $m(\tilde{b}) < 400$  GeV is excluded by a previous search from CMS [23].

## 9 Conclusion

A search for bottom-squark pairs in events with  $b$ -jets, hadronically decaying tau leptons and large missing transverse momentum is presented. A simplified SUSY model assuming  $\tilde{b} \rightarrow b\tilde{\chi}_2^0 \rightarrow bh\tilde{\chi}_1^0$  is considered, where at least one Higgs boson decays to a pair of tau leptons. This analysis has unique sensitivity at low  $\tilde{\chi}_2^0$  masses due to the presence of hadronically decaying tau leptons that mitigate the Standard Model background and to the associated tau neutrinos that add to the  $E_T^{\text{miss}}$  originating from the  $\tilde{\chi}_1^0$ . A multi-bin signal region exploiting angular correlations between the  $b$ -jets and the hadronically decaying tau leptons is used to search for a  $\tilde{b}$  signal. The data observed in the signal regions are compatible with the expected Standard Model background. Exclusion limits are placed on the bottom-squark mass at the 95% confidence level. For  $m(\tilde{\chi}_2^0)$  ranging from 130 GeV to 180 GeV, bottom-squark masses below 775 GeV to 850 GeV are excluded. This significantly extends the reach of a previous ATLAS search [22], which was performed in final states with  $b$ -jets and large  $E_T^{\text{miss}}$ , in this challenging region of parameter space.

# Appendix

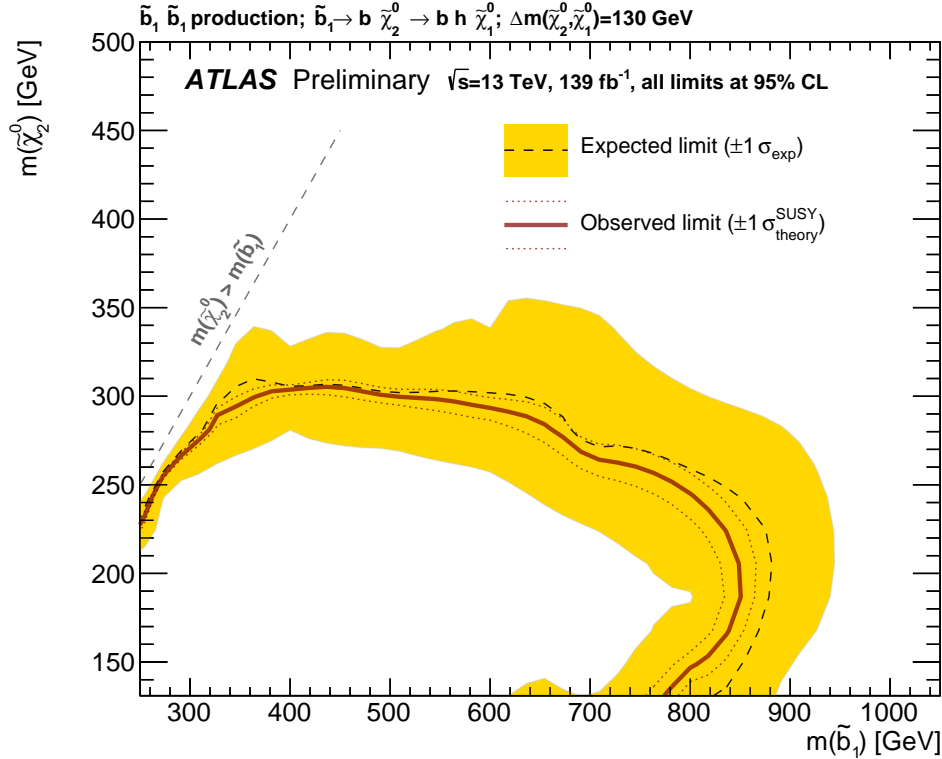


Figure 9: Expected and observed exclusion contours at the 95% CL as function of  $m(\tilde{b})$  and  $m(\tilde{\chi}_2^0)$ , assuming  $\Delta m(\tilde{\chi}_2^0, \tilde{\chi}_1^0) = 130$  GeV. Results are shown for the present search that requires hadronically decaying tau leptons,  $b$ -jets and  $E_T^{\text{miss}}$  in the final state.

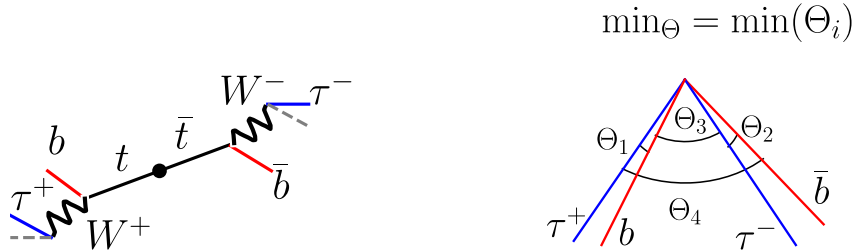


Figure 10: Schematic representation of the  $\min_{\Theta}$  variable in a  $t\bar{t}$  event with two hadronically decaying tau leptons (blue) and two  $b$ -jets (red). The dashed grey lines are the neutrinos. The left image shows the decay chain, the right image the four angles  $\Theta_i$  for all combinations of  $b$ -jets and tau leptons that  $\min_{\Theta}$  is the minimum of. (The angles  $\Theta_i$  are depicted here as all lying in the same plane, but in reality they are defined between the 3-dimensional momentum vectors.)

Table 8: Cutflow for the benchmark signal model  $(m(\tilde{b}), m(\tilde{\chi}_2^0)) = (800, 180)$  GeV. The simulated sample contains 30000 raw MC events after the generator filters are applied, which is equivalent to 152130 raw MC events before the generator filters. Weighted event yields are reported, normalized to an integrated luminosity of  $139 \text{ fb}^{-1}$ .

Selection	Weighted event yields
Preselection	198
Trigger plateau	112.7
Muon veto	102
$N_{\tau} > 1$	20.4
$\text{OS}(\tau_1, \tau_2)$	18.7
$H_T > 1100 \text{ GeV}$	13.4
$55 \text{ GeV} < m(\tau_1, \tau_2) < 120 \text{ GeV}$	10.7
$m_{T2} > 140 \text{ GeV}$	9.61
Single-bin SR $\min_{\Theta} > 0.6$	9.28
Multi-bin SR $\min_{\Theta} < 0.5$	0.08
Multi-bin SR $\min_{\Theta} \in [0.5, 1.0]$	2.47
Multi-bin SR $\min_{\Theta} > 1.0$	7.10

## References

- [1] Y. Golfand and E. Likhtman, *Extension of the Algebra of Poincare Group Generators and Violation of P Invariance*, JETP Lett. **13** (1971) 323, [Pisma Zh. Eksp. Teor. Fiz. **13** (1971) 452].
- [2] D. Volkov and V. Akulov, *Is the neutrino a goldstone particle?* Phys. Lett. B **46** (1973) 109.
- [3] J. Wess and B. Zumino, *Supergauge transformations in four dimensions*, Nucl. Phys. B **70** (1974) 39.
- [4] J. Wess and B. Zumino, *Supergauge invariant extension of quantum electrodynamics*, Nucl. Phys. B **78** (1974) 1.
- [5] S. Ferrara and B. Zumino, *Supergauge invariant Yang-Mills theories*, Nucl. Phys. B **79** (1974) 413.
- [6] A. Salam and J. Strathdee, *Super-symmetry and non-Abelian gauges*, Phys. Lett. B **51** (1974) 353.
- [7] N. Sakai, *Naturalnes in Supersymmetric Guts*, Z. Phys. C **11** (1981) 153.
- [8] S. Dimopoulos, S. Raby, and F. Wilczek, *Supersymmetry and the scale of unification*, Phys. Rev. D **24** (1981) 1681.
- [9] L. E. Ibáñez and G. G. Ross, *Low-energy predictions in supersymmetric grand unified theories*, Phys. Lett. B **105** (1981) 439.
- [10] S. Dimopoulos and H. Georgi, *Softly broken supersymmetry and SU(5)*, Nucl. Phys. B **193** (1981) 150.
- [11] G. R. Farrar and P. Fayet, *Phenomenology of the production, decay, and detection of new hadronic states associated with supersymmetry*, Phys. Lett. B **76** (1978) 575.
- [12] H. Goldberg, *Constraint on the Photino Mass from Cosmology*, Phys. Rev. Lett. **50** (1983) 1419, Erratum: Phys. Rev. Lett. **103** (2009) 099905.
- [13] J. Ellis, J. Hagelin, D. V. Nanopoulos, K. A. Olive, and M. Srednicki, *Supersymmetric relics from the big bang*, Nucl. Phys. B **238** (1984) 453.
- [14] R. Barbieri and G. Giudice, *Upper bounds on supersymmetric particle masses*, Nucl. Phys. B **306** (1988) 63.
- [15] B. de Carlos and J. Casas, *One-loop analysis of the electroweak breaking in supersymmetric models and the fine-tuning problem*, Phys. Lett. B **309** (1993) 320, arXiv: [hep-ph/9303291](#).
- [16] J. Alwall, M.-P. Le, M. Lisanti, and J. G. Wacker, *Searching for directly decaying gluinos at the Tevatron*, Phys. Lett. B **666** (2008) 34, arXiv: [0803.0019 \[hep-ph\]](#).
- [17] J. Alwall, P. Schuster, and N. Toro, *Simplified models for a first characterization of new physics at the LHC*, Phys. Rev. D **79** (2009) 075020, arXiv: [0810.3921 \[hep-ph\]](#).
- [18] D. Alves et al., *Simplified models for LHC new physics searches*, J. Phys. G **39** (2012) 105005, arXiv: [1105.2838 \[hep-ph\]](#).
- [19] P. Fayet, *Supersymmetry and Weak, Electromagnetic and Strong Interactions*, Phys. Lett. B **64** (1976) 159.
- [20] P. Fayet, *Spontaneously Broken Supersymmetric Theories of Weak, Electromagnetic and Strong Interactions*, Phys. Lett. B **69** (1977) 489.
- [21] ATLAS Collaboration, *Search for supersymmetry in events with b-tagged jets and missing transverse momentum in pp collisions at  $\sqrt{s} = 13$  TeV with the ATLAS detector*, JHEP **11** (2017) 195, arXiv: [1708.09266 \[hep-ex\]](#).

- [22] ATLAS Collaboration, *Search for bottom-squark pair production with the ATLAS detector in final states containing Higgs bosons, b-jets and missing transverse momentum*, *JHEP* **12** (2019) 060, arXiv: [1908.03122 \[hep-ex\]](https://arxiv.org/abs/1908.03122).
- [23] CMS Collaboration, *Search for supersymmetry using Higgs boson to diphoton decays at  $\sqrt{s} = 13\text{ TeV}$* , *JHEP* **11** (2019) 109, arXiv: [1908.08500 \[hep-ex\]](https://arxiv.org/abs/1908.08500).
- [24] ATLAS Collaboration, *The ATLAS Experiment at the CERN Large Hadron Collider*, *JINST* **3** (2008) S08003.
- [25] ATLAS Collaboration, *ATLAS Insertable B-Layer Technical Design Report*, ATLAS-TDR-19, 2010, URL: <https://cds.cern.ch/record/1291633>.
- [26] ATLAS Collaboration, ATLAS-TDR-19-ADD-1, 2012, URL: <https://cds.cern.ch/record/1451888>.
- [27] B. Abbott et al., *Production and integration of the ATLAS Insertable B-Layer*, *JINST* **13** (2018) T05008, arXiv: [1803.00844 \[physics.ins-det\]](https://arxiv.org/abs/1803.00844).
- [28] ATLAS Collaboration, *Luminosity determination in  $pp$  collisions at  $\sqrt{s} = 13\text{ TeV}$  using the ATLAS detector at the LHC*, ATLAS-CONF-2019-021, 2019, URL: <https://cds.cern.ch/record/2677054>.
- [29] G. Avoni et al., *The new LUCID-2 detector for luminosity measurement and monitoring in ATLAS*, *JINST* **13** (2018) P07017.
- [30] ATLAS Collaboration, *The ATLAS Simulation Infrastructure*, *Eur. Phys. J. C* **70** (2010) 823, arXiv: [1005.4568 \[physics.ins-det\]](https://arxiv.org/abs/1005.4568).
- [31] S. Agostinelli et al., *GEANT4 – a simulation toolkit*, *Nucl. Instrum. Meth. A* **506** (2003) 250.
- [32] ATLAS Collaboration, *The simulation principle and performance of the ATLAS fast calorimeter simulation FastCaloSim*, ATL-PHYS-PUB-2010-013, 2010, URL: <https://cds.cern.ch/record/1300517>.
- [33] T. Sjöstrand, S. Mrenna, and P. Skands, *A brief introduction to PYTHIA 8.1*, *Comput. Phys. Commun.* **178** (2008) 852, arXiv: [0710.3820 \[hep-ph\]](https://arxiv.org/abs/0710.3820).
- [34] R. D. Ball et al., *Parton distributions with LHC data*, *Nucl. Phys. B* **867** (2013) 244, arXiv: [1207.1303 \[hep-ph\]](https://arxiv.org/abs/1207.1303).
- [35] ATLAS Collaboration, *The Pythia 8 A3 tune description of ATLAS minimum bias and inelastic measurements incorporating the Donnachie–Landshoff diffractive model*, ATL-PHYS-PUB-2016-017, 2016, URL: <https://cds.cern.ch/record/2206965>.
- [36] E. Bothmann et al., *Event Generation with Sherpa 2.2*, *SciPost Phys.* **7** (2019) 034, arXiv: [1905.09127 \[hep-ph\]](https://arxiv.org/abs/1905.09127).
- [37] D. J. Lange, *The EvtGen particle decay simulation package*, *Nucl. Instrum. Meth. A* **462** (2001) 152.
- [38] S. Frixione, P. Nason, and G. Ridolfi, *A positive-weight next-to-leading-order Monte Carlo for heavy flavour hadroproduction*, *JHEP* **09** (2007) 126, arXiv: [0707.3088 \[hep-ph\]](https://arxiv.org/abs/0707.3088).
- [39] P. Nason, *A new method for combining NLO QCD with shower Monte Carlo algorithms*, *JHEP* **11** (2004) 040, arXiv: [hep-ph/0409146](https://arxiv.org/abs/hep-ph/0409146).
- [40] S. Frixione, P. Nason, and C. Oleari, *Matching NLO QCD computations with parton shower simulations: the POWHEG method*, *JHEP* **11** (2007) 070, arXiv: [0709.2092 \[hep-ph\]](https://arxiv.org/abs/0709.2092).

[41] S. Alioli, P. Nason, C. Oleari, and E. Re, *A general framework for implementing NLO calculations in shower Monte Carlo programs: the POWHEG BOX*, *JHEP* **06** (2010) 043, arXiv: [1002.2581](https://arxiv.org/abs/1002.2581) [hep-ph].

[42] R. D. Ball et al., *Parton distributions for the LHC run II*, *JHEP* **04** (2015) 040, arXiv: [1410.8849](https://arxiv.org/abs/1410.8849) [hep-ph].

[43] ATLAS Collaboration, *Studies on top-quark Monte Carlo modelling for Top2016*, ATL-PHYS-PUB-2016-020, 2016, URL: <https://cds.cern.ch/record/2216168>.

[44] T. Sjöstrand et al., *An introduction to PYTHIA 8.2*, *Comput. Phys. Commun.* **191** (2015) 159, arXiv: [1410.3012](https://arxiv.org/abs/1410.3012) [hep-ph].

[45] ATLAS Collaboration, *ATLAS Pythia 8 tunes to 7 TeV data*, ATL-PHYS-PUB-2014-021, 2014, URL: <https://cds.cern.ch/record/1966419>.

[46] M. Beneke, P. Falgari, S. Klein, and C. Schwinn, *Hadronic top-quark pair production with NNLL threshold resummation*, *Nucl. Phys. B* **855** (2012) 695, arXiv: [1109.1536](https://arxiv.org/abs/1109.1536) [hep-ph].

[47] M. Cacciari, M. Czakon, M. Mangano, A. Mitov, and P. Nason, *Top-pair production at hadron colliders with next-to-next-to-leading logarithmic soft-gluon resummation*, *Phys. Lett. B* **710** (2012) 612, arXiv: [1111.5869](https://arxiv.org/abs/1111.5869) [hep-ph].

[48] P. Bärnreuther, M. Czakon, and A. Mitov, *Percent-Level-Precision Physics at the Tevatron: Next-to-Next-to-Leading Order QCD Corrections to  $q\bar{q} \rightarrow t\bar{t} + X$* , *Phys. Rev. Lett.* **109** (2012) 132001, arXiv: [1204.5201](https://arxiv.org/abs/1204.5201) [hep-ph].

[49] M. Czakon and A. Mitov, *NNLO corrections to top-pair production at hadron colliders: the all-fermionic scattering channels*, *JHEP* **12** (2012) 054, arXiv: [1207.0236](https://arxiv.org/abs/1207.0236) [hep-ph].

[50] M. Czakon and A. Mitov, *NNLO corrections to top pair production at hadron colliders: the quark-gluon reaction*, *JHEP* **01** (2013) 080, arXiv: [1210.6832](https://arxiv.org/abs/1210.6832) [hep-ph].

[51] M. Czakon, P. Fiedler, and A. Mitov, *Total Top-Quark Pair-Production Cross Section at Hadron Colliders Through  $O(\alpha_S^4)$* , *Phys. Rev. Lett.* **110** (2013) 252004, arXiv: [1303.6254](https://arxiv.org/abs/1303.6254) [hep-ph].

[52] M. Czakon and A. Mitov, *Top++: A program for the calculation of the top-pair cross-section at hadron colliders*, *Comput. Phys. Commun.* **185** (2014) 2930, arXiv: [1112.5675](https://arxiv.org/abs/1112.5675) [hep-ph].

[53] E. Re, *Single-top Wt-channel production matched with parton showers using the POWHEG method*, *Eur. Phys. J. C* **71** (2011) 1547, arXiv: [1009.2450](https://arxiv.org/abs/1009.2450) [hep-ph].

[54] R. Frederix, E. Re, and P. Torrielli, *Single-top t-channel hadroproduction in the four-flavour scheme with POWHEG and aMC@NLO*, *JHEP* **09** (2012) 130, arXiv: [1207.5391](https://arxiv.org/abs/1207.5391) [hep-ph].

[55] S. Alioli, P. Nason, C. Oleari, and E. Re, *NLO single-top production matched with shower in POWHEG: s- and t-channel contributions*, *JHEP* **09** (2009) 111, arXiv: [0907.4076](https://arxiv.org/abs/0907.4076) [hep-ph], Erratum: *JHEP* **02** (2010) 011.

[56] J. Alwall et al., *The automated computation of tree-level and next-to-leading order differential cross sections, and their matching to parton shower simulations*, *JHEP* **07** (2014) 079, arXiv: [1405.0301](https://arxiv.org/abs/1405.0301) [hep-ph].

[57] T. Gleisberg and S. Höche, *Comix, a new matrix element generator*, *JHEP* **12** (2008) 039, arXiv: [0808.3674](https://arxiv.org/abs/0808.3674) [hep-ph].

[58] F. Caccioli, P. Maierhöfer, and S. Pozzorini, *Scattering Amplitudes with Open Loops*, *Phys. Rev. Lett.* **108** (2012) 111601, arXiv: [1111.5206](https://arxiv.org/abs/1111.5206) [hep-ph].

[59] A. Denner, S. Dittmaier, and L. Hofer, *Collier: A fortran-based complex one-loop library in extended regularizations*, *Comput. Phys. Commun.* **212** (2017) 220, arXiv: [1604.06792 \[hep-ph\]](https://arxiv.org/abs/1604.06792).

[60] S. Schumann and F. Krauss, *A parton shower algorithm based on Catani–Seymour dipole factorisation*, *JHEP* **03** (2008) 038, arXiv: [0709.1027 \[hep-ph\]](https://arxiv.org/abs/0709.1027).

[61] S. Höche, F. Krauss, M. Schönherr, and F. Siegert, *A critical appraisal of NLO+PS matching methods*, *JHEP* **09** (2012) 049, arXiv: [1111.1220 \[hep-ph\]](https://arxiv.org/abs/1111.1220).

[62] S. Höche, F. Krauss, M. Schönherr, and F. Siegert, *QCD matrix elements + parton showers. The NLO case*, *JHEP* **04** (2013) 027, arXiv: [1207.5030 \[hep-ph\]](https://arxiv.org/abs/1207.5030).

[63] S. Catani, F. Krauss, R. Kuhn, and B. R. Webber, *QCD Matrix Elements + Parton Showers*, *JHEP* **11** (2001) 063, arXiv: [hep-ph/0109231](https://arxiv.org/abs/hep-ph/0109231).

[64] S. Höche, F. Krauss, S. Schumann, and F. Siegert, *QCD matrix elements and truncated showers*, *JHEP* **05** (2009) 053, arXiv: [0903.1219 \[hep-ph\]](https://arxiv.org/abs/0903.1219).

[65] C. Anastasiou, L. J. Dixon, K. Melnikov, and F. Petriello, *High precision QCD at hadron colliders: Electroweak gauge boson rapidity distributions at NNLO*, *Phys. Rev. D* **69** (2004) 094008, arXiv: [hep-ph/0312266](https://arxiv.org/abs/hep-ph/0312266).

[66] L. Lönnblad, *Correcting the Colour-Dipole Cascade Model with Fixed Order Matrix Elements*, *JHEP* **05** (2002) 046, arXiv: [hep-ph/0112284](https://arxiv.org/abs/hep-ph/0112284).

[67] L. Lönnblad and S. Prestel, *Matching tree-level matrix elements with interleaved showers*, *JHEP* **03** (2012) 019, arXiv: [1109.4829 \[hep-ph\]](https://arxiv.org/abs/1109.4829).

[68] W. Beenakker, C. Borschensky, M. Krämer, A. Kulesza, and E. Laenen, *NNLL-fast: predictions for coloured supersymmetric particle production at the LHC with threshold and Coulomb resummation*, *JHEP* **12** (2016) 133, arXiv: [1607.07741 \[hep-ph\]](https://arxiv.org/abs/1607.07741).

[69] W. Beenakker et al., *NNLL Resummation for Squark-Antisquark and Gluino-Pair Production at the LHC*, *JHEP* **12** (2014) 023, arXiv: [1404.3134 \[hep-ph\]](https://arxiv.org/abs/1404.3134).

[70] W. Beenakker et al., *Towards NNLL resummation: hard matching coefficients for squark and gluino hadroproduction*, *JHEP* **10** (2013) 120, arXiv: [1304.6354 \[hep-ph\]](https://arxiv.org/abs/1304.6354).

[71] W. Beenakker et al., *NNLL resummation for squark-antisquark pair production at the LHC*, *JHEP* **01** (2012) 076, arXiv: [1110.2446 \[hep-ph\]](https://arxiv.org/abs/1110.2446).

[72] W. Beenakker et al., *Soft-gluon resummation for squark and gluino hadroproduction*, *JHEP* **12** (2009) 041, arXiv: [0909.4418 \[hep-ph\]](https://arxiv.org/abs/0909.4418).

[73] A. Kulesza and L. Motyka, *Soft gluon resummation for the production of gluino-gluino and squark-antisquark pairs at the LHC*, *Phys. Rev. D* **80** (2009) 095004, arXiv: [0905.4749 \[hep-ph\]](https://arxiv.org/abs/0905.4749).

[74] A. Kulesza and L. Motyka, *Threshold Resummation for Squark-Antisquark and Gluino-Pair Production at the LHC*, *Phys. Rev. Lett.* **102** (2009) 111802, arXiv: [0807.2405 \[hep-ph\]](https://arxiv.org/abs/0807.2405).

[75] W. Beenakker, R. Höpker, M. Spira, and P. Zerwas, *Squark and gluino production at hadron colliders*, *Nucl. Phys. B* **492** (1997) 51, arXiv: [hep-ph/9610490](https://arxiv.org/abs/hep-ph/9610490).

[76] J. Butterworth et al., *PDF4LHC recommendations for LHC Run II*, *J. Phys. G* **43** (2016) 023001, arXiv: [1510.03865 \[hep-ph\]](https://arxiv.org/abs/1510.03865).

[77] ATLAS Collaboration, *Vertex Reconstruction Performance of the ATLAS Detector at  $\sqrt{s} = 13$  TeV*, ATL-PHYS-PUB-2015-026, 2015, URL: <https://cds.cern.ch/record/2037717>.

[78] M. Cacciari, G. P. Salam, and G. Soyez, *The anti- $k_t$  jet clustering algorithm*, *JHEP* **04** (2008) 063, arXiv: [0802.1189 \[hep-ph\]](https://arxiv.org/abs/0802.1189).

[79] M. Cacciari, G. P. Salam, and G. Soyez, *FastJet user manual*, *Eur. Phys. J. C* **72** (2012) 1896, arXiv: [1111.6097 \[hep-ph\]](https://arxiv.org/abs/1111.6097).

[80] ATLAS Collaboration, *Topological cell clustering in the ATLAS calorimeters and its performance in LHC Run 1*, *Eur. Phys. J. C* **77** (2017) 490, arXiv: [1603.02934 \[hep-ex\]](https://arxiv.org/abs/1603.02934).

[81] ATLAS Collaboration, *Jet energy scale measurements and their systematic uncertainties in proton–proton collisions at  $\sqrt{s} = 13$  TeV with the ATLAS detector*, *Phys. Rev. D* **96** (2017) 072002, arXiv: [1703.09665 \[hep-ex\]](https://arxiv.org/abs/1703.09665).

[82] ATLAS Collaboration, *Selection of jets produced in 13 TeV proton–proton collisions with the ATLAS detector*, ATLAS-CONF-2015-029, 2015, URL: <https://cds.cern.ch/record/2037702>.

[83] ATLAS Collaboration, *Tagging and suppression of pileup jets with the ATLAS detector*, ATLAS-CONF-2014-018, 2014, URL: <https://cds.cern.ch/record/1700870>.

[84] ATLAS Collaboration, *ATLAS b-jet identification performance and efficiency measurement with  $t\bar{t}$  events in  $pp$  collisions at  $\sqrt{s} = 13$  TeV*, *Eur. Phys. J. C* **79** (2019) 970, arXiv: [1907.05120 \[hep-ex\]](https://arxiv.org/abs/1907.05120).

[85] ATLAS Collaboration, *Expected performance of the ATLAS b-tagging algorithms in Run-2*, ATL-PHYS-PUB-2015-022, 2015, URL: <https://cds.cern.ch/record/2037697>.

[86] ATLAS Collaboration, *Reconstruction, Energy Calibration, and Identification of Hadronically Decaying Tau Leptons in the ATLAS Experiment for Run-2 of the LHC*, ATL-PHYS-PUB-2015-045, 2015, URL: <https://cds.cern.ch/record/2064383>.

[87] T. Barillari et al., *Local Hadronic Calibration*, ATL-LARG-PUB-2009-001-2, 2008, URL: <https://cds.cern.ch/record/1112035>.

[88] ATLAS Collaboration, *Reconstruction of hadronic decay products of tau leptons with the ATLAS experiment*, *Eur. Phys. J. C* **76** (2016) 295, arXiv: [1512.05955 \[hep-ex\]](https://arxiv.org/abs/1512.05955).

[89] ATLAS Collaboration, *Identification of hadronic tau lepton decays using neural networks in the ATLAS experiment*, ATL-PHYS-PUB-2019-033, 2019, URL: <https://cds.cern.ch/record/2688062>.

[90] ATLAS Collaboration, *Measurement of the tau lepton reconstruction and identification performance in the ATLAS experiment using  $pp$  collisions at  $\sqrt{s} = 13$  TeV*, ATLAS-CONF-2017-029, 2017, URL: <https://cds.cern.ch/record/2261772>.

[91] ATLAS Collaboration, *Muon reconstruction performance of the ATLAS detector in proton–proton collision data at  $\sqrt{s} = 13$  TeV*, *Eur. Phys. J. C* **76** (2016) 292, arXiv: [1603.05598 \[hep-ex\]](https://arxiv.org/abs/1603.05598).

[92] ATLAS Collaboration, *Electron reconstruction and identification in the ATLAS experiment using the 2015 and 2016 LHC proton–proton collision data at  $\sqrt{s} = 13$  TeV*, *Eur. Phys. J. C* **79** (2019) 639, arXiv: [1902.04655 \[hep-ex\]](https://arxiv.org/abs/1902.04655).

[93] ATLAS Collaboration,  *$E_T^{\text{miss}}$  performance in the ATLAS detector using 2015–2016 LHC  $pp$  collisions*, ATLAS-CONF-2018-023, 2018, URL: <https://cds.cern.ch/record/2625233>.

[94] ATLAS Collaboration, *Performance of the missing transverse momentum triggers for the ATLAS detector during Run-2 data taking*, submitted to JHEP (2020), arXiv: [2005.09554 \[hep-ex\]](https://arxiv.org/abs/2005.09554).

- [95] G. Cowan, K. Cranmer, E. Gross, and O. Vitells, *Asymptotic formulae for likelihood-based tests of new physics*, *Eur. Phys. J. C* **71** (2011) 1554, arXiv: [1007.1727 \[physics.data-an\]](https://arxiv.org/abs/1007.1727), Erratum: *Eur. Phys. J. C* **73** (2013) 2501.
- [96] C. G. Lester and D. J. Summers, *Measuring masses of semi-invisibly decaying particles pair produced at hadron colliders*, *Phys. Lett. B* **463** (1999) 99, arXiv: [hep-ph/9906349 \[hep-ph\]](https://arxiv.org/abs/hep-ph/9906349).
- [97] C. G. Lester and B. Nachman, *Bisection-based asymmetric  $M_{T2}$  computation: a higher precision calculator than existing symmetric methods*, *JHEP* **03** (2015) 100, arXiv: [1411.4312 \[hep-ph\]](https://arxiv.org/abs/1411.4312).
- [98] M. Baak et al., *HistFitter software framework for statistical data analysis*, *Eur. Phys. J. C* **75** (2015) 153, arXiv: [1410.1280 \[hep-ex\]](https://arxiv.org/abs/1410.1280).
- [99] ATLAS Collaboration, *Search for squarks and gluinos with the ATLAS detector in final states with jets and missing transverse momentum using  $4.7\text{fb}^{-1}$  of  $\sqrt{s} = 7\text{ TeV}$  proton–proton collision data*, *Phys. Rev. D* **87** (2013) 012008, arXiv: [1208.0949 \[hep-ex\]](https://arxiv.org/abs/1208.0949).
- [100] ATLAS Collaboration, *Jet energy resolution in proton–proton collisions at  $\sqrt{s} = 7\text{ TeV}$  recorded in 2010 with the ATLAS detector*, *Eur. Phys. J. C* **73** (2013) 2306, arXiv: [1210.6210 \[hep-ex\]](https://arxiv.org/abs/1210.6210).
- [101] ATLAS Collaboration, *Measurement of  $b$ -tagging efficiency of  $c$ -jets in  $t\bar{t}$  events using a likelihood approach with the ATLAS detector*, ATLAS-CONF-2018-001, 2018, URL: <https://cds.cern.ch/record/2306649>.
- [102] ATLAS Collaboration, *Calibration of light-flavour  $b$ -jet mistagging rates using ATLAS proton–proton collision data at  $\sqrt{s} = 13\text{ TeV}$* , ATLAS-CONF-2018-006, 2018, URL: <https://cds.cern.ch/record/2314418>.
- [103] ATLAS Collaboration, *Improvements in  $t\bar{t}$  modelling using NLO+PS Monte Carlo generators for Run 2*, ATL-PHYS-PUB-2018-009, 2018, URL: <https://cds.cern.ch/record/2630327>.
- [104] S. Frixione, E. Laenen, P. Motylinski, C. D. White, and B. R. Webber, *Single-top hadroproduction in association with a  $W$  boson*, *JHEP* **07** (2008) 029, arXiv: [0805.3067 \[hep-ph\]](https://arxiv.org/abs/0805.3067).
- [105] A. L. Read, *Presentation of search results: the  $CL_S$  technique*, *J. Phys. G* **28** (2002) 2693.